

Key Points:

- A size-resolving floc model embedded in a large eddy simulation model is used to study flocculation in shallow-water Langmuir turbulence
- Flocculation processes modify vertical mean concentration profiles for flocs of a certain size
- Langmuir turbulence modulates aggregation and breakup rates

Supporting Information:

- Supporting Information S1

Correspondence to:

J.-H. Liang,
jliang@lsu.edu

Citation:

Liu, J., Liang, J.-H., Xu, K., Chen, Q., Chen, Q., & Ozdemir, C. E. (2019). Modeling sediment flocculation in langmuir turbulence. *Journal of Geophysical Research: Oceans*, 124. <https://doi.org/10.1029/2019JC015197>

Received 4 APR 2019

Accepted 14 OCT 2019

Accepted article online 31 OCT 2019

Modeling Sediment Flocculation in Langmuir Turbulence

Jinliang Liu¹ , Jun-Hong Liang^{1,2,3} , Kehui Xu^{1,3} , Qin Chen⁴ , and Celalettin Emre Ozdemir^{2,3,5} 

¹Department of Oceanography and Coastal Sciences, Louisiana State University and A. & M. College, Baton Rouge, LA, USA, ²Center for Computation and Technology, Louisiana State University and A. & M. College, Baton Rouge, LA, USA, ³Coastal Studies Institute, Louisiana State University and A. & M. College, Baton Rouge, LA, USA, ⁴Department of Civil and Environmental Engineering, Northeastern University, Boston, MA, USA, ⁵Department of Civil and Environmental Engineering, Louisiana State University and A. & M. College, Baton Rouge, LA, USA

Abstract Cohesive sediments exist as flocs of different sizes, which are built and destroyed through flocculation processes including both aggregation and breakup. This study investigates sediment flocculation processes in wave-driven Langmuir turbulence that is commonly observed in coastal ocean through embedding a size-resolving flocculation model into a turbulence-resolving hydrodynamic model. The specific research questions are how Langmuir turbulence affects flocculation processes and how flocculation processes impact the spatial and size distributions of suspended cohesive sediment. The results show that Langmuir turbulence suspends flocs in the water column and organizes flocs of different sizes. By modulating the encounter of flocs and redistributing flocs in the turbulence field, Langmuir turbulence enhances the aggregation and breakup rates of flocs that are located in similar regions with high turbulent dissipation rates and suppresses those of others. As an outcome of modulated flocculation processes, floc size distribution changes with depth and floc mass concentration profiles change with floc size. The addition of wave breaking increases the shear rate near the surface and reduces the median floc size and averaged settling velocity, leading to increase in total floc mass concentration in the whole water column. Wave breaking also increases cross-shelf sediment transport by more than 15% under the simulated conditions, which is comparable to that due to Langmuir turbulence compared to shear turbulence. Both floc size distribution and floc concentration vary with wind and wave conditions.

1. Introduction

The transport of suspended sediment in the coastal ocean plays an important role not only in shaping coastal topography (e.g., Schwab et al., 2013) but also in a variety of problems in oceanography related to ocean color remote sensing (D'Sa et al., 2018), coral reef ecology (Bannister et al., 2012), oxygen and nutrient dynamics (Moriarty et al., 2018), and the sequestration of aquatic pollutants such as spilled oil (Passow et al., 2012). In sediment transport modeling, settling velocity is one of the key parameters (e.g., Chen et al., 2010; Dyer, 1989; Geyer et al., 2004; Harris & Wiberg, 2002; Harris et al., 2005; Sherwood et al., 2018). Sediments can be characterized as noncohesive and cohesive. For noncohesive sediment with negligible impact of electrochemical or biochemical attraction (Son & Hsu, 2011), primarily composed of sand and gravel-sized material (Shrestha & Blumberg, 2005), the settling velocity is mainly controlled by the physical properties including particle size, shape, and density (e.g., Dietrich, 1982; Ferguson & Church, 2004; Rubey, 1933). In contrast, for cohesive sediment, which is primarily the fine-grained mixture including silt, clay, fine sand, and organic matter, the additional cohesive characteristic due to electrochemical or biochemical attraction enables individual sediment particles to stick together to form an agglomeration of mineral and/or organic particles called floc or aggregate (Maggi, 2005; Mehta, 2013; Son & Hsu, 2011; Winterwerp & Van, 2004). Flocculation processes, which include aggregation and breakup, increase the complexity in determining the settling velocity and other properties (e.g., size, shape, and density) of cohesive sediment (e.g., Droppo et al., 2004; Dyer, 1989; Droppo, 2006; Mehta, 2013; Strom & Keyvani, 2011; Winterwerp & Van, 2004). Flocculation processes are also important for suspended sediment concentration (SSC) in the water column available for horizontal transport (e.g., Droppo et al., 1998; Sherwood et al., 2018; Verney et al., 2011). Therefore, an accurate prediction of cohesive sediment transport requires a better understanding of flocculation processes.

Aggregation refers to the physical process forming the flocs through bonding of smaller aggregates and primary (clay) mineral particles (Mehta, 2013; Son & Hsu, 2011; Strom and Keyvani, 2016). The rate of aggregation is dependent on the frequency that particles collide, particle size, salinity, and pH (e.g., Burd & Jackson, 2009; Mietta et al., 2009; Winterwerp, 1998). As aggregation causes the growth of sediment flocs, it also reduces the residence time of sediment particles in the water column (Burd & Jackson, 2009). Breakup refers to the separation of parent flocs into primary particles or smaller daughter flocs by turbulent shear or interparticle collision (Dyer, 1989; Son & Hsu, 2011), and is inversely related to yield strength of the floc (e.g., Son & Hsu, 2011; Verney et al., 2011; Winterwerp, 1998).

Flocculation processes have been studied through field observation, laboratory experiments, and numerical models. Particularly, a series of laboratory and field studies (e.g., Braithwaite et al., 2012; Keyvani & Strom, 2014; Strom & Keyvani, 2016) have been conducted to establish the relationship between flocculation processes and turbulent shear rate (defined as $G = \sqrt{\epsilon/v} = v/\eta^2$, with ϵ the turbulent kinetic energy dissipation rate, v the kinematic viscosity, and η the Kolmogorov length scale Kolmogorov, 1941). Turbulence not only increases the growth rate of flocs by enhancing interparticle collision but also increases breakup rate by increasing the shear stress on the floc. Braithwaite et al. (2012) measured the characteristics of turbulence and suspended particles in an energetic tidal channel for multiple tidal cycles, and found that over each tidal cycle, the median particle size varies approximately by a factor of 3, with the largest particles observed during low turbulence environment at slack water. Keyvani and Strom (2014) examined the effect of repeated cycles of high and low shear rates on the equilibrium floc size in a laboratory mixing chamber and found that the final equilibrium floc size in the experiment depends only on the turbulent shear rate. Strom and Keyvani (2016) measured the transient evolution of floc size in a decaying shear field representative of generic conditions in an extended river mouth plume. They found that median floc size in decaying turbulence is smaller than the equilibrium median floc size under the same shear rate. In addition to shear rate (G), other factors including fractal dimension, floc yield strength, salinity, pH, biological content, and SSC also affect flocculation processes (e.g., Maggi, 2007; Mietta et al., 2009; Son & Hsu, 2009; Tran et al., 2018). Maggi (2007) proposed a power law function based on laboratory data to describe the decreasing fractal dimension with floc size during floc growth and showed that the aggregation and breakup rates can change to a factor of 2 or more compared to models with constant fractal dimension. Based on observations in a variety of shear rate, pH, salinity, and organic matter content, Mietta et al. (2009) found that the median floc size increases as the salinity increases in saline suspension at pH = 8 and also increases with increasing organic matter content if other conditions are identical. Son and Hsu (2009) derived an analytic formulation for variable floc yield strength and incorporated it into a flocculation model with variable fractal dimension, with improved performance in predicting temporal evolution of floc size. Tran et al. (2018) investigated the evolution of floc size under both steady and decaying concentration conditions when turbulent shear rate remains constant in laboratory mixing tanks, and found that under steady concentration condition, the equilibrium floc size linearly increases with concentration (within the range 50–400 mg/L), but the dependence is weak at high shear rate ($G = 50 \text{ s}^{-1}$). They also found that floc sizes drop quickly as a response to decay in concentration at high shear rate ($G = 50 \text{ s}^{-1}$).

Floc size distribution (FSD) is an important indicator to quantitatively examine the effect of flocculation processes, since its temporal variation stores the dynamical information on participating flocs in the flocculation processes and sediment transport (Lee et al., 2012; Shen & Maa, 2017). For instance, bimodal FSD with one peak at clay/silt size and the other at sand size indicates either the aggregation of silt and/or clay or intense erosion events of sand (Lee et al., 2012). Moreover, for realistic sediment modeling, knowledge of FSD is important for the selection of subordinate unimodal lognormal FSDs (e.g., Lee et al., 2012; Shen, Lee, et al., 2018; Shen, Toorman, et al., 2018), and the median floc size (D_{50}), which is a crucial parameter.

Flocculation models have been developed based on theoretical considerations and laboratory experiments and can be categorized into three types. The first is the single-size model: It describes the rate of change in floc size through a linear combination of aggregation and breakup rate terms in a Lagrangian framework and allows a characteristic floc size (e.g., median floc size) dynamically evolve with various turbulent shear rates and initial sediment concentration (e.g., Winterwerp, 1998). The second is the model based upon a predefined sediment distribution (Maerz & Wirtz, 2009). The second model assumes that particle size distribution follows an exponential distribution and calculates the temporal variation of the average floc size

under various shear rate conditions. This type of model has a small number of state variables, which is efficient when coupled with large-scale biogeochemical models (Maerz et al., 2011). The third type of model is based on the population balance equations (PBEs, or size class-based model; e.g., Verney et al., 2011). This type of model calculates the concentration of multiple sediment sizes, allowing the dynamic evolution of FSD. The first two types of models are relatively easy to solve, but their applicability is restricted to unimodal sediment size distribution and cannot be extended to investigate the dynamic evolution of a bimodal distribution (e.g., Benson & French, 2007). Flocculation models have been coupled with hydrodynamic models to study flocculation processes in estuarine and coastal environments (e.g., Son & Hsu, 2011; Shen et al., 2018a; Shen et al., 2018b; Sherwood et al., 2018; Winterwerp, 2002; Xu et al., 2008, 2010). Winterwerp (2002) implemented a single-size flocculation model (Winterwerp, 1998) in a one-dimensional vertical model to reproduce the vertical profiles of SSC observed in a turbidity maximum in the Ems estuary. Xu et al. (2008) implemented a size-resolving PBEs model in a one-dimensional vertical model. The same authors applied the model in the three-dimensional Princeton Ocean Model to simulate fine-grained particle trapping in an estuarine turbidity maximum (ETM) of the Upper Chesapeake Bay. In the same study, it was shown that flocculation processes are the main mechanisms to cause strong tidally asymmetric SSC. Son and Hsu (2011) incorporated a single-size flocculation model that allows variable fractal dimension and floc yield strength (Son & Hsu, 2009) in a one-dimensional vertical model to simulate cohesive sediment suspension in the Ems/Dollard estuary. They found that variable critical shear stress is necessary to accurately represent the sediment supply from the bed. Lee et al. (2011) developed a two-class PBEs model to simulate the bimodal flocculation of marine or estuarine sediments. Shen et al. (2018a) improved Lee et al. (2011)'s model to a three-class PBEs model coupled with the three-dimensional TELEMAC-3D (Janin et al., 1992) and later applied the model to investigate the biomediated flocculation in Belgian coasts (Shen et al., 2018b). Recently, the flocculation model (FLOCMOD) developed by Verney et al. (2011) was implemented in the Coupled Ocean-Atmosphere-Wave-Sediment Transport (COAWST) Modeling System (Warner et al., 2010), and was applied in a test case of a two-dimensional salt-wedge estuary to examine the cohesive sediment deposits beneath the ETM (Sherwood et al., 2018). The simulation showed that the ETM with floc dynamics extended further upstream and had much smaller SSC in the bottom layer compared to that without floc dynamics.

Our study focuses on flocculation processes and their effects on the distribution of suspended sediment in wave-driven Langmuir circulations (LC; or Langmuir turbulence) that span entire water, over shallow continental shelf. Langmuir circulations are along-wind counterrotating vortex pairs and arise from the interaction between ocean surface gravity waves and wind-driven currents (D'Asaro, 2014; Leibovich, 1983). They influence the flocculation processes of sediments in two ways: One is through modifying turbulent shear rate (G) in the water column, and the other is through redistributing sediments. To our best knowledge, no study has examined flocculation processes in Langmuir turbulence that is distinctly different from turbulent flows in laboratory environment. The specific objectives of this study are (1) to develop a coupled-turbulence-flocculation model which resolves the floc size and concentration distributions in continental shelf, (2) to examine the effect of Langmuir turbulence as well as wave breaking on flocculation processes, and (3) to study the effect of flocculation processes on the fate of suspended cohesive sediment transport due to Langmuir turbulence. The rest of the paper is organized as follows. Section 2 describes the coupled-turbulence-flocculation model and its configuration. Section 3 presents the results of a benchmark model run that includes flocculation processes, wave-driven Langmuir turbulence, and wave breaking. Section 4 discusses the effects of wave breaking, turbulence type, erosion fluxes, and settling velocities on floc distribution through comparing results from benchmark case and those from systematically varying different processes. Section 5 is conclusions.

2. Model Description and Configuration

2.1. Model Description

A coupled large eddy simulation (LES) floc model is developed. The model resolves the three-dimensional turbulence structure, temporal and spatial variations of floc size and concentration. The details of this model are described in this section.

2.1.1. LES Model

Turbulent flow in the oceanic surface boundary layer is simulated using the National Center for Atmospheric Research LES model (McWilliams et al., 1997; Sullivan & McWilliams, 2010). The model solves the filtered

wave-averaged Navier-Stokes equations (e.g., McWilliams et al., 2012; Suzuki & Fox-Kemper, 2016):

$$\frac{\partial u_i}{\partial t} = -\frac{\partial u_i u_j}{\partial x_j} - \frac{\partial \pi}{\partial x_i} + \epsilon_{ijk} u_j^{St} \omega_k - \frac{\partial \tau_{ij}}{\partial x_j}, \quad (1)$$

$$\frac{\partial e}{\partial t} = -u_j \frac{\partial e}{\partial x_j} - u_j^{St} \frac{\partial e}{\partial x_j} - \tau_{ij} S_{ij} - \tau_{ij} \frac{\partial u_i^{St}}{\partial x_j} + \frac{\partial}{\partial x_j} (2\nu_t \frac{\partial e}{\partial x_j}) - \epsilon + W^q, \quad (2)$$

where $u_j = (u, v, w)$ are the resolved (filtered) velocity components along x (downwind), y (crosswind), and z (positive upward) directions, respectively; ϵ_{ijk} is the Levi-Civita symbol; $\pi = \frac{p}{\rho_0} + \frac{2}{3}e + \frac{1}{2}[(u_j + u_j^{St})^2 - u_j u_j]$ is the generalized pressure field (e.g., Sullivan et al. 2007) with resolved pressure p , and Stokes drift $u_j^{St} = (u^{St}, 0, 0)$ along x , y , and z directions, respectively; e is the subgrid-scale (SGS) turbulent kinetic energy calculated following Sullivan et al. (2007); the SGS viscosity is calculated without the near-surface correction (Sullivan et al., 1994); $(\omega_x, \omega_y, \omega_z) = \nabla \times (u, v, w)$ are the resolved vorticities; τ_{ij} are the SGS fluxes related to the SGS turbulent kinetic energy using equation (2) (Sullivan et al., 1994); and instantaneous turbulent kinetic energy dissipation rate ϵ is calculated following Sullivan et al. (1994) (see their equation (11)). The seawater density is assumed constant in this study. While wave breaking is not explicitly simulated, its integral effect on turbulent kinetic energy is modeled as input forcing W^q that is obtained by using the stochastic breaking wave model of Sullivan et al. (2007). In the breaking wave model, the breaking wave energy flux (W^q in equation (2)) is calculated using the formula proposed by Terray et al. (1996) and is a function of wind stress and wave age. Similar approach has been used in McWilliams et al. (2012).

The model has been extensively applied to study the ocean surface boundary layer turbulence driven by a variety of surface and lateral boundary conditions (e.g., Hamlington et al., 2014; Harcourt, 2015; Liu et al., 2018; McWilliams et al., 2012, 2014; Sullivan et al., 2012; Van Roekel et al., 2012) and produces results that agree with in situ observation (e.g., Fan et al., 2018; Liang et al., 2017). It has also been applied to study neutrally (e.g., Smith et al., 2016) and positively buoyant tracers (e.g., Brunner et al., 2015; Liang et al., 2018).

2.1.2. Sediment Model With Flocculation Processes

The balance equation for the mass density of flocs based on the Smoluchowski framework (Burd & Jackson, 2009; Jackson & Burd, 2015; Von, 1916) is as follows:

$$\begin{aligned} \frac{\partial F(\vec{x}, \Gamma, t)}{\partial t} = & \frac{1}{2} \int_{\Gamma_0}^{\Gamma} \frac{m^2}{m_s^2 m'} F(\vec{x}, \Gamma_s, t) \mathcal{K}(\Gamma_s, \Gamma') F(\vec{x}, \Gamma', t) d\Gamma' \\ & - \int_{\Gamma_0}^{\infty} \frac{1}{m'} F(\vec{x}, \Gamma, t) \mathcal{K}(\Gamma, \Gamma') F(\vec{x}, \Gamma', t) d\Gamma' \\ & + \int_{\Gamma}^{\infty} \frac{m}{m'} Q(\Gamma, \Gamma') \mathcal{P}(\Gamma') F(\vec{x}, \Gamma', t) d\Gamma' - F(\vec{x}, \Gamma, t) \mathcal{P}(\Gamma) \\ & - \frac{\partial}{\partial x_j} ((u_j + u_j^{St}) F(\vec{x}, \Gamma, t)) - \frac{\partial \tau_{jF}}{\partial x_j} + \frac{\partial w_s F(\vec{x}, \Gamma, t)}{\partial x_3}, \end{aligned} \quad (3)$$

where $F(\vec{x}, \Gamma, t)$ is the mass density function (Berry, 1967) at spatial position $\vec{x} = (x, y, z)$ and time t for mass grid $\Gamma = \ln r$ with r the radius of flocs of mass m (see equation (13) for the relationship between Γ and m), Γ_0 is the first mass grid, \mathcal{K} is the aggregation kernel that describes the rate of floc collision, Q is the size distribution of daughter flocs, \mathcal{P} is the breakup frequency, and w_s is the settling velocity of the floc. For the flocs of mass m , the first term on the right-hand side (RHS) of equation (3) represents the increase in the flocs due to the aggregation of flocs of mass m_s and m' ($m = m_s + m'$); the second term represents the decrease in the flocs due to aggregation with flocs of other sizes; the third term represents the increase in the flocs due to breakup of larger flocs; and the fourth term represents the decrease in the flocs due to breakup per se. The rest of terms on the RHS represents advection, SGS diffusion (Sullivan et al., 1996), and settling of flocs, respectively. As shown in section 4, the mean floc mass concentration in the water column is below $\mathcal{O}(1) \text{ g L}^{-1}$, and therefore, the interaction between sediment and turbulence (e.g., Ozdemir et al., 2010) is ignored. The balance equations for multisize particulate tracers have previously been implemented in the LES model to study gas bubbles (Liang et al., 2011, 2012, 2013).

Aggregation occurs when particles collide. There are mainly three collision mechanisms: Brownian motion, differential settling, and the effect of turbulent flows (e.g., Maggi, 2005; Winterwerp, 1998). Random motions of particles can cause the mutual collision (Brownian motion). Settling flocs with higher settling velocity are

able to sweep the small suspended flocs with lower settling velocity to the bed while growing/diminishing in size (differential settling) (e.g., Lick et al., 1993; McCave, 1984). The flocs carried by the turbulent eddies may collide with other flocs in the water column. The last among the three is the most important in estuaries and coastal areas (Winterwerp, 1998). The aggregation kernel \mathcal{K} in equation (3) (unit: $\text{m}^3 \text{s}^{-1}$) is a linear combination of Brownian motion, differential settling, and turbulent shear effects (Burd & Jackson, 1997; Maggi, 2005):

$$\mathcal{K} = \alpha_{i,j}(\mathcal{K}_B + \mathcal{K}_D + \mathcal{K}_T), \quad (4)$$

with

$$\mathcal{K}_B = \frac{2}{3} \frac{k_B T_a}{\mu} \frac{(r_i + r_j)^2}{r_i r_j}, \quad (5)$$

$$\mathcal{K}_D = \pi (r_i + r_j)^2 |w_i^s - w_j^s|, \quad (6)$$

$$\mathcal{K}_T = \frac{4}{3} G (r_i + r_j)^3, \quad (7)$$

where $\alpha_{i,j}$ is the collision efficiency (the probability that flocs would aggregate during collision) (Droppo et al., 2004); \mathcal{K}_B , \mathcal{K}_D , and \mathcal{K}_T are the collision rates due to Brownian motion, differential settling, and turbulence shear (Hill et al., 2001; Maggi, 2005), respectively; k_B is the Boltzmann constant; T_a is the absolute temperature; r_i and r_j are the radius of flocs in size bin i and j , respectively; w_i^s and w_j^s are the settling velocity of flocs in size bin i and j , respectively (Xu et al., 2008). While the collision efficiency is usually assumed as a constant in previous studies (e.g., Verney et al., 2011; Xu et al., 2008), here it is calculated as a function of floc size and shear rate following Soos et al. (2007) to account for the hydrodynamic effect due to floc size (e.g., Bäbler et al., 2006; Kusters, 1991):

$$\alpha_{i,j} = \alpha_{1,1} \frac{\exp(-A_1(1 - \frac{r_i}{r_j})^2)}{\left(\frac{r_i r_j}{r_1^2}\right)^{A_2}} \exp\left(-\left(\frac{r_i + r_j}{A_4}\right)^{A_3}\right) G^{-A_5} \quad (8)$$

where $\alpha_{1,1}$ is the aggregation rate prefactor for doublet formation (Kusters, 1991; Soos et al., 2007), and values of parameters (A_1 , A_2 , A_3 , A_4 , and A_5) are estimated by fitting the model to the published laboratory experimental data at equilibrium state (see the appendix and cf. Table 1 in Soos et al., 2007). The effect of Brownian motion is negligible in estuaries and coastal regions (e.g., McCave, 1984; van Leussen, 1994). The effect of differential settling is important only when turbulence is weak and is mostly observed during slack tide (e.g., Eisma & Li, 1993; Lick et al., 1993). Therefore, the effects of Brownian motion and differential settling are not considered in this study (i.e., $K_B = 0$ and $K_D = 0$) (e.g., Verney et al., 2011; Xu et al., 2008).

Settling velocity w_s is calculated as a function of floc size following Sternberg et al. (1999):

$$w_{s,j} = 0.0002(D_j)^{1.54}, \quad (9)$$

where D_j is the floc diameter in μm and $w_{s,j}$ in mm s^{-1} . Here equation (9) is the best fitting curve between the measured settling velocity and suspended floc size obtained from in situ observation, whereby the sediment sample contained approximately 67% silt and 23% clay (Sternberg et al., 1999). The measurement was taken in relatively low turbidity ($\sim 70 \text{ mg L}^{-1}$ at 100 cmab (cm above bed)) and energetic flow (an average current speed of 11.6 cm s^{-1} at 100 cmab and a mean tidal range of 1.4 m) environments (Ogston & Sternberg, 1999). Similar relationship between the observed settling velocity and floc size has also been reported in other relatively low turbidity environments (e.g., Hill et al., 1998; Mikkelsen et al., 2007). In this study, the simulated median floc size in the benchmark run is between $200 \mu\text{m}$ and $300 \mu\text{m}$ and is within the size range (130 – $740 \mu\text{m}$) of particles used to derive equation (9) (Sternberg et al., 1999). Equation (9) implicitly includes the effect of fractal structure of flocs on the floc density. However, we are not able to obtain the actual fractal dimension from this observation taken in the realistic turbulent environment, and we assumed fractal dimension is 2.0 following previous studies (e.g., Xu et al., 2008). Alternative relationships between settling velocity and floc size are available in the literature, with modifications for the fractal structure of flocculated sediment (e.g., Khelifa & Hill, 2006; Strom & Keyvani, 2011; Winterwerp, 2002). Sensitivity tests on settling

velocity are conducted in this study (section 4.3), since small uncertainties in the floc size can lead to significant differences, which are as large as 2–3 order of magnitude, in settling velocity measured from both fields and laboratory (e.g., Strom & Keyvani, 2011).

The breakup frequency \mathcal{P} (unit: s^{-1}) is calculated as (Xu et al., 2008):

$$\mathcal{P}_i = \frac{\mathcal{E}}{N_f} G \left(\frac{\tau_t}{\tau_y} \right)^{\varphi_i} \left(\frac{r_i - r_1}{r_1} \right)^{3-N_f} \quad (10)$$

where \mathcal{E} is a tunable breakup parameter (see Table A2); $\tau_t = \mu G$ is the turbulence-induced shear stress, with μ the dynamic viscosity; $\tau_y = F_y / 4r_i^2$ is the strength of the floc, with $F_y \approx 10^{-10}$ N the estimated yield strength (Winterwerp, 1998; Xu et al., 2008); N_f is the fractal dimension, and φ_i the power of the ratio of (τ_t/τ_y) . Breakup frequency increases with parameter φ_i . In Xu et al. (2008), φ_i is 0.5. In this study, a modification on the coefficient φ_i is applied following Kuprenas et al. (2018) considering that the equilibrium size of flocs is limited by the Kolmogorov length scale:

$$\varphi_i = C_1 + C_2 \frac{D_i}{\eta}, \quad (11)$$

where C_1 and C_2 are constant, D_i is the diameter of the floc with mass m_i , and $\eta = (\nu^3/\epsilon)^{1/4}$ is the Kolmogorov length scale (Kolmogorov, 1941). Equation (11) reduces to $\varphi \equiv C_1 \equiv 0.5$, similar to equation (3) in Xu et al. (2008) when $D_i \ll \eta$. The second term on the RHS of equation (11) leads to a significant increase in breakup frequency when D_i approaches η (Kuprenas et al., 2018), which results in better comparison with laboratory measurements.

The binary breakup is used as the size distribution of daughter flocs in this study, which is defined as (Zhang & Li, 2003) follows:

$$Q(\Gamma, \Gamma') = \begin{cases} 2, & \text{when } m = \frac{m'}{2}, \\ 0, & \text{otherwise.} \end{cases} \quad (12)$$

The effect of the size distribution of daughter flocs on floc dynamics has been investigated theoretically and numerically (e.g., Maggi, 2005; Spicer & Pratsinis, 1996; Zhang & Li, 2003). Zhang and Li (2003) tested three types of distribution functions of daughter flocs including binary, ternary, and normal distributions and found that the choice of distribution function of daughter flocs did not cause significant difference in the steady-state FSD. Sensitivity tests showed that ternary breakup leads to smaller median floc size (less than 15%) compared to that due to binary breakup, consistent with the results of Zhang and Li (2003).

The mass of floc in each size bin i (diameter D_i) is calculated as (Kranenburg, 1994) follows:

$$m_i = \rho_s \frac{\pi}{6} D_p^3 \left(\frac{D_i}{D_p} \right)^{N_f}, \quad (13)$$

where $\rho_s = 2,650 \text{ kg m}^{-3}$ is the density of primary particle and D_p is the diameter of the primary particles. Equation (13) includes the effect of fractal structure of the flocs. Primary particles are the individual particles that have a size range 0.25–4 μm (Shen et al., 2018a). In this study, the diameter of primary particle in this study is selected as 0.5 μm ($D_p = 0.5 \mu\text{m}$), which is uniform in our computations.

The density of floc in size bin i is calculated following the relation proposed by Kranenburg (1994):

$$\rho_{f,i} = \rho + (\rho_s - \rho) \left(\frac{D_p}{D_i} \right)^{3-N_f}, \quad (14)$$

where $\rho_{f,i}$ is the density of floc in size bin i and ρ is the density of seawater.

Following Xu et al. (2008), equation (3) is discretized on a logarithmically equidistant mass grid:

$$m_{k+1} = \lambda m_k, \quad k = 1, \dots, n, \quad (15)$$

where n is the total number of bins for floc size spectrum and $\lambda = 2$ meaning floc mass doubles every size bin. Thus, the interval between Γ grid is a constant, that is, $\Delta \Gamma_k = d(\ln r) = \ln r_{k+1} - \ln r_k = \ln \lambda / N_f$. The values

for parameters in flocculation models are still under debates (e.g., Burd & Jackson, 2009; Son & Hsu, 2009; Verney et al., 2011; Xu et al., 2008). Here we select the parameters (Table A2) based on the best comparisons we obtain by comparison with available laboratory results (Table A1).

Zero-flux boundary condition is imposed at the surface for equation (3), and the bottom boundary condition is specified as erodible seabed, whereby the net vertical sediment flux at the seabed is the difference between the erosion ($E_{s,i}$) and deposition ($E_{d,i}$) fluxes. Erosion flux is calculated following Ariathurai and Arulanandan (1978):

$$E_{s,i} = E_0(1 - \phi) \frac{\tau_{sf} - \tau_{cr,i}}{\tau_{cr,i}}, \text{ if } \tau_{sf} > \tau_{cr,i} \quad (16)$$

where for each floc size bin i , E_s is the surface erosion mass flux ($\text{kg m}^{-2} \text{s}^{-1}$), E_0 is the bed erodibility ($\text{kg m}^{-2} \text{s}^{-1}$), ϕ is the porosity, τ_{cr} is the critical shear stress (Pa) calculated following Soulsby et al. (1997), and τ_{sf} is the total skin friction bottom stress (Pa) calculated following Warner et al. (2008). The fraction of each sediment class is evaluated from published in situ observation in an inner-shelf region (Law et al., 2008, T35 in Figure 3B), and interpolated into each size bin.

Deposition flux is calculated as follows:

$$E_{d,i} = w_{s,i} C_i, \quad (17)$$

where C_i is the mass concentration of floc in size bin i at the bottommost grid cell. Equation (17) implies the assumption that there is no concentration gradient in the bottommost computing grid. The assumption is valid for large particles and may not be true for fine particles (e.g., Sanford & Halka, 1993). Equation (17) also suggests that the deposition flux is dependent on the vertical resolution of the bottommost grid since the bottom boundary layer often shows high gradients in C_i (e.g., Sherwood et al., 2018; Warner et al., 2008; Schulz & Umlauf, 2016). However, this does not qualitatively affect the model results.

To avoid the unphysical oscillation in scalar field associated with the use of spectral method and retain the high accuracy of pseudospectral method for the velocity field, a hybrid spectral/finite-volume scheme (Chamecki et al., 2008) is implemented in the National Center for Atmospheric Research LES model for this study. In the scheme, tracer equation is discretized on a finite-volume grid, and dynamic equation is discretized on a pseudospectral and finite-difference grid and then interpolated to the finite-volume grid for tracer equation. Here we briefly describe the procedure by Chamecki et al. (2008) for velocity interpolation (only horizontal components needed for interpolation because of the staggered grid for velocity) from the spectral grid onto the finite-volume grid. The local derivatives (e.g., $\frac{\Delta U}{\Delta x}$ and $\frac{\Delta V}{\Delta x}$, where U and V are the horizontal velocity components at the center of the cell faces) are calculated using the nonlocal (spectral) derivatives (e.g., $(\frac{\partial u}{\partial x})^{\text{spec}}$ and $(\frac{\partial v}{\partial x})^{\text{spec}}$) instead of the spectral velocity field (u and v), which makes the conservation of mass satisfied on the finite-volume grid. Applying the above scheme to all the cells along the horizontal direction given that the interpolated velocities (U and V) are shared by the two neighboring cells, a linear system of equations for interpolated horizontal velocity are obtained, and can be solved by imposing the average of interpolated horizontal velocity with the averaged original (u and v) velocity along the same direction (for more details, refer to Chamecki et al., 2008). The tracer equation is simulated by finite-volume method with the advection term using the bounded third-order upwind interpolation scheme SMART (Gaskell & Lau, 1988) following the implementation approach by Waterson and Deconinck (2007). The hybrid spectral/finite-volume scheme has been applied to study the evolution of spilled oil in ocean surface boundary layer turbulence by Yang et al. (2015).

2.2. Model Configuration

The model is configured on a rectangular computational domain of $100 \text{ m} \times 100 \text{ m} \times 15 \text{ m}$ with $100 \times 100 \times 96$ grids. The horizontal grids are evenly spaced and the vertical grids are stretched with the finest resolution close to both boundaries. Increase in grid resolution and domain size does not change the flow dynamics. The time step is dynamically determined by the Courant-Friedrichs-Lowy condition (Sullivan et al., 1996). In this paper, we choose 10 m s^{-1} as the wind speed at 10 m above the surface, corresponding to a wind stress (τ) of 0.159 N m^{-2} , and a surface friction velocity (u_s) of 0.0126 m s^{-1} , using the drag law by Liu et al. (1979). No-slip boundary condition is applied at the bottom. Earth's rotation is not considered following previous LES studies of coastal ocean turbulence (e.g., Grosch & Gargett, 2016; Tejada-Martinez & Grosch, 2007). There are 27 floc size bins ranging from $0.5 \mu\text{m}$ to $4096 \mu\text{m}$, with floc

Table 1
Model Configuration for Different Simulations

Case	Flocculation	Wave breaking	Langmuir turbulence	Erodibility E_0 [$\times 10^{-4}$ kg m $^{-2}$ s $^{-1}$]	Settling velocity W_s [m s $^{-1}$]
BM	Included	Included	Included	5	Equation (9)
B1	—	Included	Included	5	Equation (9)
B2	Included	—	Included	5	Equation (9)
B3	Included	Included	—	5	Equation (9)
S1	Included	Included	Included	0.5	Equation (9)
S2	Included	Included	Included	50	Equation (9)
S3	Included	Included	Included	5	$0.1 \times$ Equation (9)
S4	Included	Included	Included	5	$10 \times$ Equation (9)

Note. The benchmark experiment (Case BM) includes flocculation processes, and is driven by both wind and equilibrium wind wave including wave breaking. Cases B1, B2, and B3 are the experiments excluding flocculation processes, wave breaking, and wave-driven Langmuir turbulence, respectively. Cases S1 and S2 are the sensitivity tests on erosion fluxes. Cases S3 and S4 are the sensitivity tests on settling velocities. Em dash (—) denotes processes that are excluded.

density ranging from 2,650.0 kg m $^{-3}$ to 1,025.7 kg m $^{-3}$. The density of the primary particle ($D_p = 0.5 \mu\text{m}$) is 2,650.0 kg m $^{-3}$. Flocs are assumed to be composed of primary particles, and mass of flocs larger than the maximum bin size is added to the largest size bin. In our simulations, further increase in the largest floc size does not affect the results. A series of simulations are conducted to assess their individual role on floc size and spatial distributions, and are summarized in Table 1. The benchmark experiment (Case BM) includes flocculation processes and is driven by both wind and equilibrium wind wave including wave breaking. Case B1, B2, and B3 are the experiments that exclude flocculation processes, wave breaking, and wave-driven Langmuir turbulence, respectively. As mentioned previously, parametric sensitivity tests are conducted due to inherent uncertainty in the adopted flocculation model. Cases S1 and S2 are the sensitivity tests on erosion fluxes by decreasing/increasing the erodibility by a factor of 10, respectively. Cases S3 and S4 are the sensitivity tests on settling velocities through decreasing/increasing the settling velocities by a factor of 10, respectively. Only one factor was changed in each sensitivity test, while other model parameters are kept the same as those in the benchmark case. The initial suspended mass concentration is set to 0 for all size bins. The water column is well mixed. All the simulations start from a fully turbulent field, which comes from a spin-up run without flocs. All the statistics are averaged over 10 hr after equilibrium is reached. The turbulent Langmuir number [$La = (u_*/u_s)^{1/2}$, $u_s = u^{St}(0)$] is 0.31 for wave-driven Langmuir case, and the Stokes drift $u^{St}(z)$ is calculated based on linear wave theory without shallow or deep water approximation (see equation (3) in Lentz & Fewings, 2012). The wavelength is 24.94 m with significant wave height $H_s = 1.63$ m and peak wave period $T_p = 4.0$ s.

3. Results

To understand the effect of flocculation processes on floc distribution, we begin the analysis by first examining the instantaneous flow field and floc distribution (section 3.1), followed by statistical moments of total floc mass concentration (section 3.2) in the benchmark case (Case BM), which gives an overview on how wave-driven Langmuir turbulence affects the spatial distribution of flocs. The moments are based on temporal and horizontal average and denoted by angle brackets ($\langle \rangle$), including the mean, variance, and skewness for floc mass concentration. Then the size and vertical distributions of floc mass (section 3.3) are presented to demonstrate the effects of flocculation processes on FSD as well as spatial distribution of floc mass. Budget profiles of floc mass concentration are shown to interpret the role of flocculation processes (section 3.4). The effects of turbulence on aggregation and breakup rates are discussed in the end (section 3.5). For the convenience of analysis, a resolved field ψ is decomposed into a temporal average over horizontal (both x and y) directions $\langle \psi \rangle$, and the deviation (ψ') from $\langle \psi \rangle$, that is, $\psi = \langle \psi \rangle + \psi'$; average of ψ over the water column is denoted by subscript v , that is, $\psi_v = \frac{1}{|h|} \int_h^0 \langle \psi \rangle dz$, where $|h|$ is the water depth (15 m) of the computational domain; and a variable normalized by its depth-averaged value is denoted by hat, that is, $\hat{\psi} = \psi / \psi_v$. We use $C_i = \mathcal{F}_i \cdot d \ln r$ to denote the mass concentration (g L $^{-1}$) of flocs in individual size bin i , and use C_s to indicate the SSC, that is, the sum of floc mass concentration for all size bins.

3.1. Instantaneous Fields of Vertical Velocity and Floc Mass Concentration

Langmuir turbulence in shallow water has been extensively investigated in existing studies (e.g., Kukulka et al., 2012; Shrestha et al., 2018; Tejada-Martinez & Grosch, 2007). We here show only the instantaneous

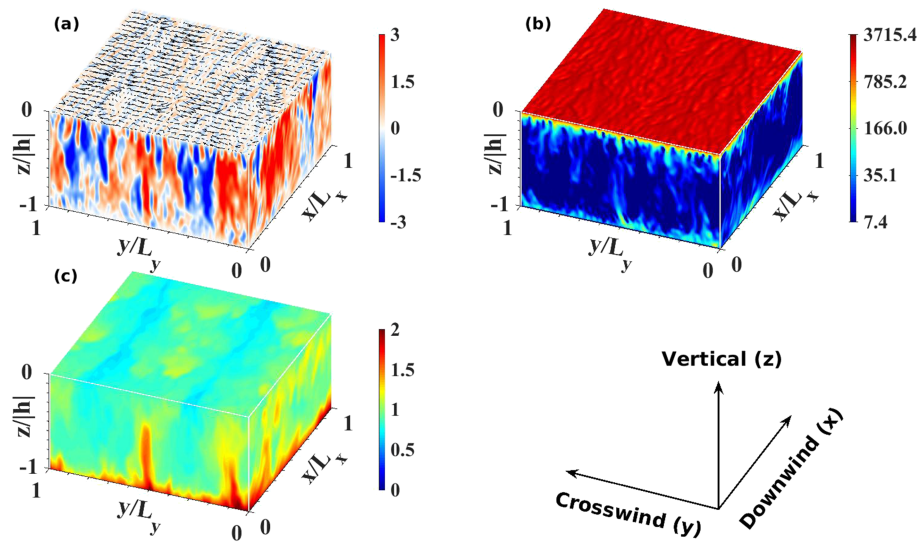


Figure 1. Three-dimensional instantaneous snapshots of (a) normalized vertical velocity (w/u_*), (b) normalized dissipation rate ($\epsilon|h|/u_*^3$), and (c) normalized total floc mass concentration including all size bins ($C/C_{s,v}$, where $C_{s,v}$ is the depth-averaged total floc mass concentration) in Case BM. The vertical depth (z) is normalized by $|h|$, while L_x and L_y are the lengths of the computational domain along downwind (x) and crosswind (y) directions, respectively. The arrow in panel (a) indicates the deviation of horizontal velocity from the average over the horizontal plane.

snapshots of normalized vertical velocity (w/u_*) (Figure 1a, and also see Figure S1 in the supporting information) and normalized turbulent kinetic energy dissipation rate (ϵ , referred to as dissipation rate for short hereafter, normalized by $u_*^3/|h|$) (Figure 1b) in Langmuir turbulence to facilitate the discussion of its effect on flocculation processes. The full-depth wave-driven Langmuir cells are shown as alternating downward (negative) and upward (positive) vertical velocities in y - z plane and streaks of downward velocities in x - y plane (Figure 1a). In addition, there are enhanced downwind flows close to the seabed below the downwelling branch (not shown), consistent with previous studies (e.g., Gargett & Wells, 2007). The presence of wave breaking greatly increases the dissipation rate (ϵ) mainly near the surface, at which the dissipation rate is higher in the downwelling region than that in the upwelling region (cf. Figures 1a and 1b). The dissipation rate away from both boundaries is relatively low compared to that close to the surface and seabed (Figure 1b). Therefore, turbulent shear rate ($G = \sqrt{\epsilon/v}$, here ϵ is the local value calculated from the LES model) is spatially nonuniform in Langmuir turbulence, different from the homogeneous turbulence in a laboratory experiment. High turbulent shear rate increases both the floc collision rate (equation (7)) and breakup frequency (equation (10)), which leads to the change in floc size and spatial distributions, in addition to the rates of aggregation and breakup. When the Langmuir circulation occupies the entire water depth, the near-bed convergence zone below the upwelling branch serves to sweep suspended sediments into downwind rows along the seabed. Some of the collected suspended sediments are mixed into the water column by the upwelling flow. Consequently, higher total concentration of suspended sediments (Figure 1c) is in the form of upwelling plume and collocates with the upward branch of Langmuir circulation that reaches the seabed, consistent with previous observations (Gargett et al., 2004).

Figure 2a shows the near-bed instantaneous snapshot of normalized total floc mass concentration ($\hat{C}_s(x, y) = C_s(x, y)/C_{s,v}$). Floc distribution in Langmuir turbulence is strongly nonhomogeneous and is different from the usual laboratory setting where flocs are well mixed. Near the seabed, suspended flocs are mainly concentrated in the stripes in the downwind direction. The stripes are located in the near-bed convergence zone (below the upwelling branch of Langmuir circulation), characterized by the transitional region between positive and negative normalized crosswind velocity fluctuation (v'/u_*), for example, at around $y/L_y = 0.5$ (L_y is the length of the computation domain along crosswind direction) in Figure 2b. The total floc mass concentration is relatively small in the near-bed divergence zone (below the downwelling branch of Langmuir circulation), indicated by the transitional region between negative and positive normalized crosswind velocity fluctuation (e.g., at approximately $y/L_y = 0.75$). The horizontal distribution of floc mass concentration is different for different floc sizes. For instance, the horizontal distribution of primary particles ($D_p = 0.5 \mu\text{m}$, Figure 2c) are more homogeneous near the seabed than other flocs (Figures 2d–2f). This

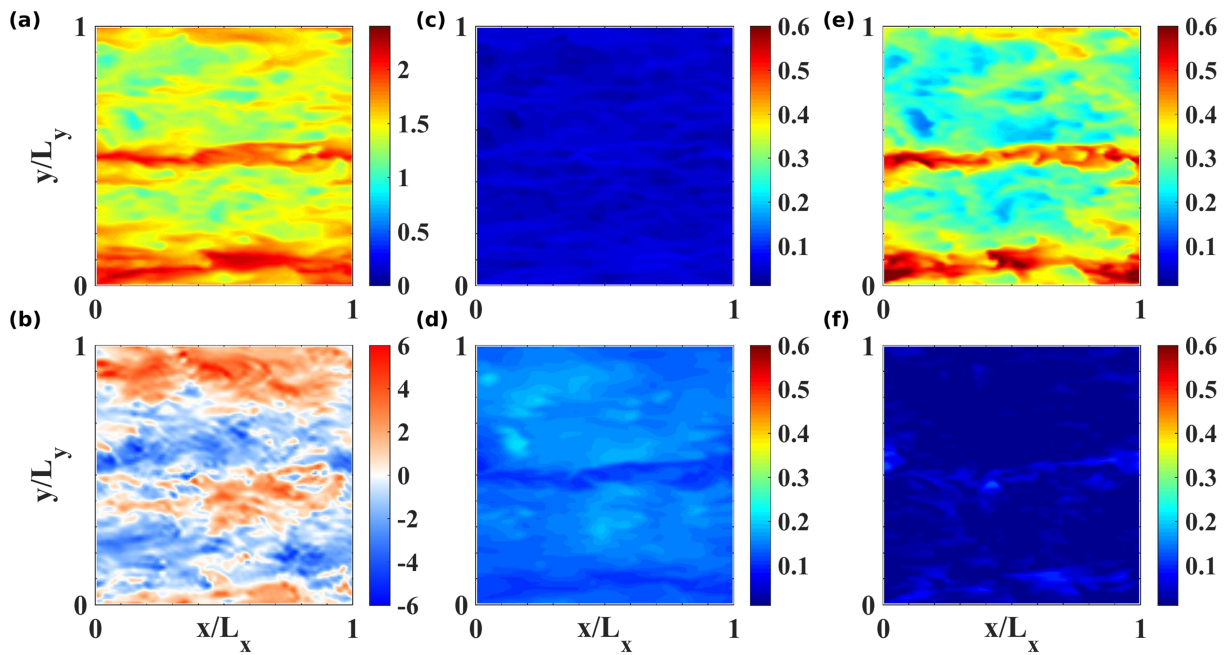


Figure 2. Two-dimensional instantaneous (x - y plane) near-bed ($z = -14.85$ m, that is, 0.15 m above the seabed) snapshots of (a) normalized total floc mass concentration ($\hat{C}_s(x, y) = C_s(x, y)/C_{s,v}$, where $C_{s,v}$ is the depth-averaged total floc mass concentration), (b) normalized crosswind velocity fluctuation ($v'(x, y)/u_*$), and normalized floc mass concentration ($C(x, y)/C_{s,v}$) in individual size bin, including: (c) $D = 0.5 \mu\text{m}$, (d) $D = 181.0 \mu\text{m}$, (e) $D = 362.0 \mu\text{m}$, and (f) $D = 724.1 \mu\text{m}$ in Case BM. Here L_x and L_y are the lengths of the computational domain along downwind (x) and crosswind (y) directions, respectively.

is mainly because primary particles have larger erosion flux and smaller settling velocity than other flocs. Since the largest size of flocs eroded from the seabed is $90.5 \mu\text{m}$ in the benchmark case (the erosion flux in individual size bin is available in Figure S4 in the supporting information), local concentration of flocs larger than $90.5 \mu\text{m}$ (e.g., $D = 181.0 \mu\text{m}$ in Figure 2d) is determined by the aggregation of smaller flocs, breakup of larger flocs, floc settling, and transport due to Langmuir turbulence. In addition, higher total number of flocs in the near-bed convergence zone leads to more floc collisions and potential for faster growth of flocs and thus larger median floc size than that in the near-bed divergence zone. Therefore, concentration for $D = 181.0 \mu\text{m}$ (Figure 2d) is smaller than that for $D = 362.0 \mu\text{m}$ (Figure 2e) in the near-bed convergence zone but is larger in the near-bed divergence zone. For flocs even larger (e.g., $D = 724.1 \mu\text{m}$ in Figure 2f), they settle to the seabed rapidly due to fast settling velocity. Since they are more easily to be torn apart by turbulent eddies, the mass concentration for $D = 724.1 \mu\text{m}$ is small and there is a large gap of low concentration between near-bed convergence zones.

The size-dependent horizontal nonhomogeneity of floc mass concentration due to Langmuir turbulence and flocculation processes is important for the transport of nutrients (e.g., Moriarty et al., 2018) and pollutants (e.g., Passow et al., 2012) in coastal areas, because it is possible that those materials attached to flocs of different sizes can either be trapped in the near-bed region, or suspended into upper column through upwelling plumes by full-depth Langmuir turbulence and transported toward the shoreline by onshore currents. The depth-dependent flocculation dynamics in Langmuir turbulence is also important for the vertical distribution of frazil ice (e.g., Drucker et al., 2003) and phytoplankton (e.g., Dierssen et al., 2009), which may further affect the light penetration and carbon export.

3.2. Statistics of Floc Mass Concentration

In this subsection, profiles of concentration statistics are used to characterize the floc distribution in Langmuir turbulence. The normalized total floc mass concentration ($\langle \hat{C}_s \rangle = \langle C_s \rangle / C_{s,v}$) is the lowest near the surface ($z/|h| > -0.1$) and is the highest near the seabed ($z/|h| < -0.9$) (Figure 3a). Away from both boundaries ($-0.9 \leq z/|h| \leq -0.1$), $\langle \hat{C}_s \rangle$ is generally uniform (Figure 3a). The total concentration in the midregion can be as high as approximately two thirds of that near the seabed, which results from strong nonlocal vertical mixing due to coherent LC structures (Figures 1a and 1c). The normalized variance of total floc mass concentration ($\langle \hat{C}_{s'}^2 \rangle = \langle C_{s'}^2 \rangle / C_{s,v}^2$) is the smallest near the surface and is the largest near the seabed

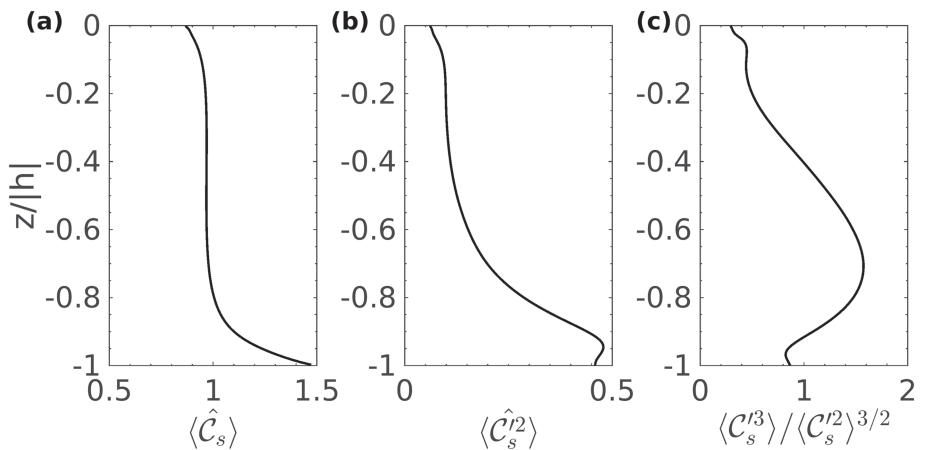


Figure 3. Vertical profiles of (a) normalized mean floc mass concentration ($\langle \hat{C}_s \rangle = \langle C_s \rangle / C_{s,v}$, where $C_{s,v}$ is the depth-averaged total floc mass concentration), (b) normalized variance of floc mass concentration fluctuation ($\langle \hat{C}_s'^2 \rangle = \langle C_s'^2 \rangle / C_{s,v}^2$), and (c) skewness of floc mass concentration fluctuation ($\langle \hat{C}_s'^3 \rangle / \langle \hat{C}_s'^2 \rangle^{3/2}$). Vertical axis is the depth normalized by $|h|$.

(Figure 3b), implying that floc mass is horizontally more homogeneous near the seabed than away from it. The skewness ($\langle \hat{C}_s'^3 \rangle / \langle \hat{C}_s'^2 \rangle^{3/2}$) of total floc mass concentration is positive throughout the water column (Figure 3c), indicating the region of low concentration is broader than the region of high concentration (Figure 1c).

3.3. Size and Vertical Distributions of Floc Mass

Figure 4a shows vertical profiles of FSD. There are three regions that have different FSDs due to difference in hydrodynamic conditions (e.g., dissipation rate ϵ , Figure 1b): (1) near-surface region ($z/|h| > -0.1$) where the median floc size is smaller than that away from the surface because of the enhanced dissipation rate (or shear rate) due to wave breaking; (2) near-bed region ($z/|h| < -0.9$) where the median floc size is larger than that in near-surface region as a result of smaller dissipation rate; and (3) midregion ($-0.9 \leq z/|h| \leq -0.1$) where the median floc size is larger than that near the surface and seabed because dissipation rate is relatively low compared to that in the other two regions (vertical profile of mean dissipation rate is available in Figure S5 in the supporting information).

Although normalized total floc mass concentration is small near the surface and large near the seabed (Figure 3a), similar to the vertical distribution of noncohesive sediment without flocculation processes (e.g., Warner et al., 2008), the profile of normalized mean mass concentration of flocs in individual size bin ($\langle \hat{C}_i \rangle = \langle C_i \rangle / C_{i,v}$, where $C_{i,v}$ is the depth-averaged mass concentration in corresponding size bin i) can be very different from that of total flocs ($\langle \hat{C}_s \rangle$) because FSD changes with depth (Figure 4a). For primary particles, $\langle \hat{C}_i \rangle$ increases with depth (Figure 4b). The value of $\langle \hat{C}_i \rangle$ in the upper part of the water column is less than 10% of that near the seabed. The large difference in $\langle \hat{C}_i \rangle$ between the midregion and near-bed region is a result of source from bed erosion. Without the bed source, the distribution would be uniform with depth as settling speed for the primary particles is small ($\sim 6.9 \times 10^{-5} \text{ mm s}^{-1}$). For $D = 16.0 \mu\text{m}$ (Figure 4c), $\langle \hat{C}_i \rangle$ profile is similar to that of primary particles. For both $D = 90.5 \mu\text{m}$ (Figure 4d) and $D = 181.0 \mu\text{m}$ (Figure 4e), $\langle \hat{C}_i \rangle$ near the surface is higher than that in the midregion. For $D = 362.0 \mu\text{m}$ (Figure 4f), there is a sharp gradient in $\langle \hat{C}_i \rangle$ near the surface as the dominant floc size near the surface is smaller than $300.0 \mu\text{m}$ (Figure 4a). For $D = 724.1 \mu\text{m}$, $\langle \hat{C}_i \rangle$ is smaller near the surface and seabed and is relatively high and more uniform in the midregion (Figure 4g), because smaller shear rate (G) in the midregion leads to increase in larger flocs.

When flocculation processes are not considered (Case B1), the shape of $\langle \hat{C}_i \rangle$ profile is similar for all floc size bins, and $\langle \hat{C}_i \rangle$ increases with water depth (not shown). For flocs larger than $90.5 \mu\text{m}$, the mass concentrations are zero without flocculation processes (Case B1) as no source from bed erosion available. In this regime, the concentration distribution mainly depends on the flow structure, settling velocity, and bed erosion. When flocculation processes are considered, however, not only the concentrations for flocs (larger than $90.5 \mu\text{m}$) are nonzero, but also $\langle \hat{C}_i \rangle$ profiles are reshaped (Figures 4e–4g). The aggregation of smaller flocs contribute to the growth of larger flocs, which have higher settling velocity and thus sink to the seabed more rapidly. In this

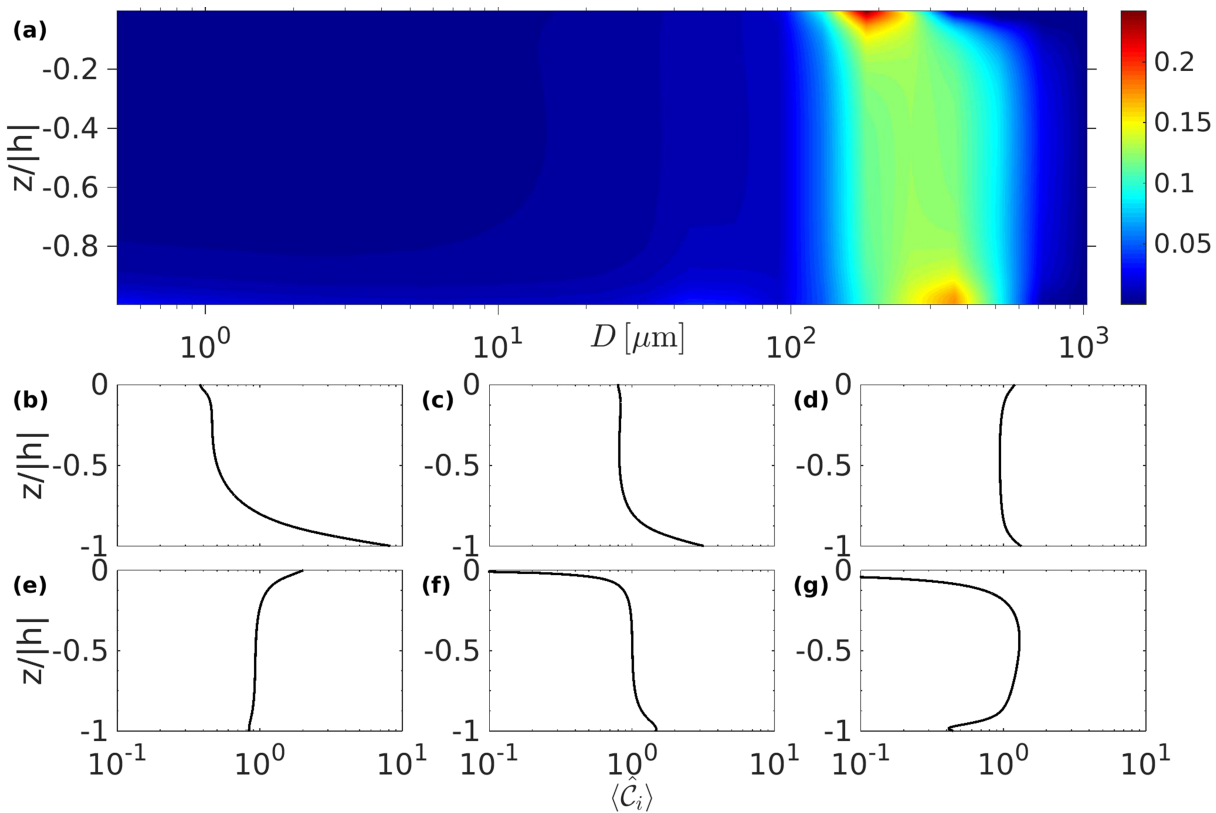


Figure 4. (a) Vertical distribution of horizontal mean floc mass density $\langle F_i \rangle$ [g L⁻¹ dln r⁻¹] in individual size bin in Case BM. Vertical profiles of normalized horizontal mean concentration ($\langle \hat{C}_i \rangle = \langle C_i \rangle / C_{i,v}$) with floc size of: (b) 0.5 μm ; (c) 16.0 μm ; (d) 90.5 μm ; (e) 181.0 μm ; (f) 362.0 μm ; and (g) 724.1 μm in Case BM. Vertical axis is the depth normalized by $|h|$.

regime, the vertical profile of floc mass concentration is affected by the competition between aggregation, breakup, turbulent transport, and floc settling, which will be discussed in next section.

We then examine the effect of flocculation processes on the vertical distribution of floc number density ($n = F_i / m_f$) [number m⁻³ dln r⁻¹] (Figure 5). Although primary particles have the largest number density in the water column, its mass concentration is relatively low because of small floc mass. Near the seabed, higher floc number density for $D \leq 90.5 \mu\text{m}$ is primarily due to bed erosion. Large number density also suggests the potential for collision and the higher aggregation rate for small flocs. In addition, the higher number concentration for flocs of $100.0 \mu\text{m} < D < 200.0 \mu\text{m}$ compared to larger flocs near the surface suggests that higher shear rate near the surface reduces large flocs and increases small flocs.

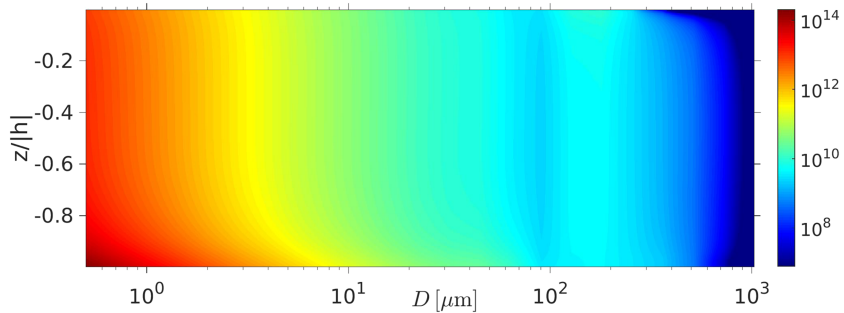


Figure 5. Vertical variation of floc number density n [number m⁻³ dln r⁻¹] in individual size bin in Case BM. Vertical axis is the depth normalized by $|h|$.

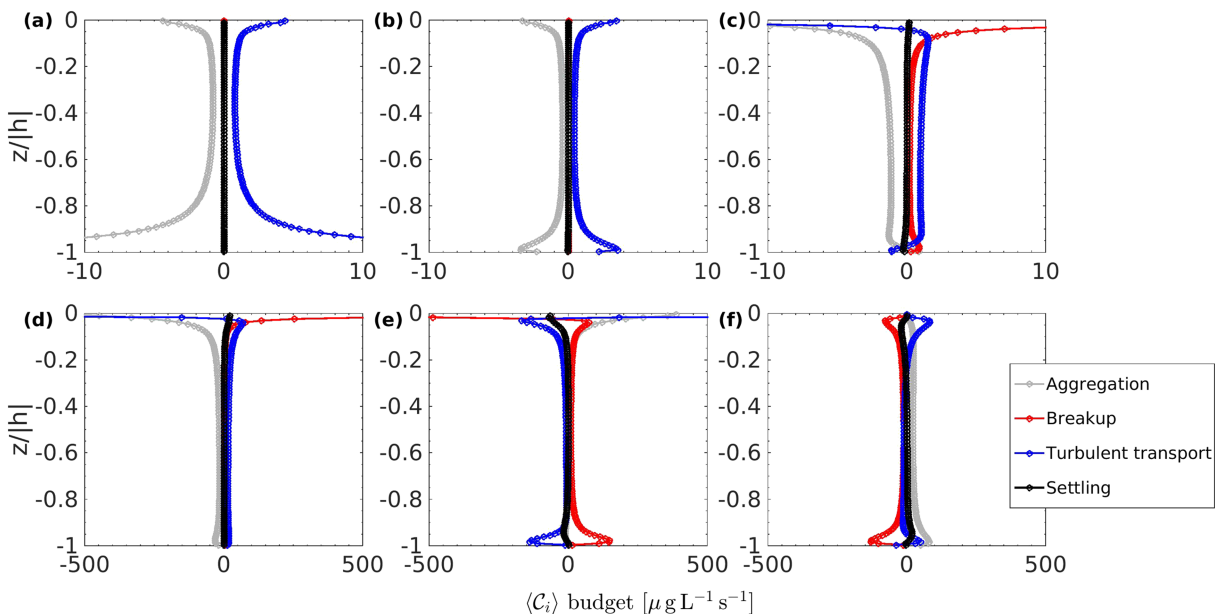


Figure 6. Vertical profiles of horizontally average floc mass concentration ($\langle C_i \rangle$) budget from aggregation (gray, see the first term on the LHS of equation (18)), breakup (red, see the second term on the LHS of equation (18)), turbulent transport (the third term on LHS of equation (18), blue), and settling (the fourth term on LHS of equation (18), black) with floc size of: (a) 0.5 μm ; (b) 16.0 μm ; (c) 90.5 μm ; (d) 181.0 μm ; (e) 362.0 μm ; and (f) 724.1 μm for Case BM. Vertical axis is the depth normalized by $|h|$.

In summary, the variability of FSD when flocculation processes are considered suggests the impact of hydrodynamic conditions (e.g., shear rate) on flocculation processes and thus the equilibrium floc size. Particularly, the near-surface, near-bed, and midregion exhibit different hydrodynamic and suspended cohesive sediment characteristics. Therefore, in Langmuir turbulence, the FSDs need to be analyzed at different depths in order to better represent the size distribution characteristics of suspended cohesive sediment in the water column.

3.4. Floc Mass Concentration Budget

The floc mass budget is examined to understand the role of flocculation and transport processes in floc distribution. After averaging equation (3) both in time and x - y plane, we can rewrite the budget equation as follows:

$$\mathcal{A} + \mathcal{B} - \left\langle \frac{\partial}{\partial x_j} (u_j \mathcal{F} + \tau_{jF}) \right\rangle + \left\langle \frac{\partial w_s \mathcal{F}(\vec{x}, \Gamma, t)}{\partial x_3} \right\rangle = 0, \quad (18)$$

where \mathcal{A} represents the effect of aggregation (i.e., the temporal and horizontal average of the first two terms on the RHS of equation (3)); \mathcal{B} represents the effect of breakup (i.e., the temporal and horizontal average of the third and fourth terms on the RHS of equation (3)); the third term on the left-hand side represents the contribution due to turbulent transport (resolved+SGS); and the last term on the left-hand side denotes the contribution due to floc settling.

Flocculation processes play different roles in the distribution of flocs of different sizes at different depths (Figure 6). The dominant balance for primary particle (Figure 4a) is between the sink due to aggregation and the source due to turbulent transport associated with Langmuir turbulence throughout the water column (Figure 6a). The aggregation sink is the largest close to the seabed where floc number concentration is the highest (Figure 5) and is relatively low in the water column. Close to the surface, dissipation rate is substantially larger than in the water column (Figure 1b), leading to higher aggregation rate than in the water column. The contributions of floc breakup and settling are negligibly small compared to the other two processes. Since binary breakup is assumed, only flocs that are slightly larger than primary particle contribute to the breakup source. Eddies that can break up those flocs have to be smaller than 0.7 μm and is uncommon in the water column given the Kolmogorov scale in the ocean is $56 \sim 10^4 \mu\text{m}$ (based on the dissipation rate $10^{-10} \sim 10^{-1} \text{ m}^2 \text{ s}^{-3}$, Thorpe 2005). The budget for flocs of diameter between 10 μm and 20 μm (referred

to as flocculi in van Leussen 1994, Lee et al. 2012) is similar to that for primary particles, and the contributions of floc breakup and settling are negligible as well (Figure 4b). This is consistent with observations showing that flocculi, which are the basic clay-based building blocks of flocs besides primary particles, are relatively stable and hardly break up even at a coastal region with high turbulent shear (Lee et al., 2012; van Leussen, 1994). The four processes play different roles in the water column for flocs of $D = 90.5 \mu\text{m}$ (Figure 4c). Near the seabed ($z/|h| < -0.95$), aggregation is the primary source and is balanced by turbulent transport. Flocs of this size aggregate more slowly than smaller flocs because their number density is smaller (Figure 5). Flocs formed from aggregation of smaller flocs are mixed into the water column by turbulence. Away from the seabed, aggregation is the primary sink and is balanced by turbulent transport. Near the surface ($z/|h| > -0.05$), the source due to breakup is larger than smaller flocs, indicating larger flocs broke apart by the eddies. For $D = 181.0 \mu\text{m}$ (Figure 4d), the breakup source is much larger than the smaller flocs and is balanced by aggregation and turbulent transport close to the surface ($z/|h| > -0.05$). Away from the surface ($z/|h| < -0.1$), the breakup source decreases dramatically, while aggregation is the primary sink and is balanced by turbulent transport. For $D = 362.0 \mu\text{m}$ (Figure 4e), breakup is the primary sink and is balanced by aggregation and turbulent transport close to the surface ($z/|h| > -0.05$). Close to the seabed ($z/|h| < -0.90$), the breakup source is much larger than that in the midregion, which is from the breakup of larger flocs and is balanced by transport sink. Away from the surface ($-0.80 < z/|h| < -0.20$), breakup is the primary source and is balanced by turbulent transport. For $D = 724.1 \mu\text{m}$ (Figure 6f), both aggregation and breakup are negligible due to small number concentration at the surface. Away from the surface and seabed ($-0.9 < z/|h| < -0.1$), breakup is the primary sink and is balanced by aggregation source. Settling of flocs is a sink in the upper column ($z/|h| > -0.4$) and is a source in the lower column ($z/|h| < -0.6$). Overall, the vertical distribution of flocs is an outcome of turbulent transport, floc settling, and flocculation processes. The presence of aggregation and breakup whose roles vary with floc size and depth modifies the contributions of turbulent transport and floc settling.

3.5. Turbulence Effects on Aggregation and Breakup Rates

In Langmuir turbulence, both turbulent dissipation rate and floc mass concentration are spatially nonuniform and temporally evolving. Under the combined effect of turbulent transport and flocculation processes, flocs of some sizes are preferentially accumulated at the regions of high dissipation rate while flocs of other sizes are mostly dispersed at regions of low dissipation rate (Figures 1b and 1c and Figures 2c–2f). For instance, flocs of $D = 362.0 \mu\text{m}$ are concentrated in the near-bed convergence zone, while flocs of $D = 181.0 \mu\text{m}$ are dispersed outside the convergence zone (Figures 2d and 2e). This implies that turbulence either enhances or suppresses flocculation processes, by modulating the encounter of flocs and by redistributing flocs in the turbulence field. The preferential accumulation of flocs of different sizes due to nonhomogeneous turbulent mixing and flocculation processes is similar to the segregation of chemically reactive species due to a heterogeneous surface forcing in the atmospheric boundary layer (e.g., Ouwersloot et al., 2011). In order to quantify the turbulence effect on aggregation rate, we define the ratio of aggregation rate \mathcal{R}_A :

$$\mathcal{R}_A = \frac{1}{|h|} \int_h^0 \frac{\langle \mathcal{F}_i \mathcal{K} \mathcal{F}_j \rangle}{\langle \mathcal{F}_i \rangle \langle \mathcal{K} \rangle \langle \mathcal{F}_j \rangle} dz = \frac{1}{|h|} \int_h^0 \frac{\langle C_i \mathcal{K} C_j \rangle}{\langle C_i \rangle \langle \mathcal{K} \rangle \langle C_j \rangle} dz, \quad (19)$$

where $\langle C_i \rangle$ and $\langle C_j \rangle$ are the horizontally averaged mass concentration of flocs in size bin i and j , respectively; and the numerator of the integrand represents the aggregation rate for flocs of size bin i and j when turbulence is resolved, while the denominator represents the scenario when turbulence is unresolved, such as in that in a regional ocean model (e.g., COAWST).

Contour of \mathcal{R}_A at equilibrium with floc size in Case BM is shown in Figure 7a. Here $\mathcal{R}_A = 1$ refers to no difference in aggregation rate due to turbulence. The region of $\mathcal{R}_A < 1$ (e.g., when $100 \mu\text{m} < D_i < 200 \mu\text{m}$ and $D_j > 300 \mu\text{m}$, where D_i and D_j are the diameters of two flocs that aggregate, respectively) suggests that the aggregation rate between the two floc sizes is suppressed by turbulence. This is mainly because flocs within the given size range are not at the same spatial locations as other sizes. For instance, in the lower water column, flocs with $D_i > 300 \mu\text{m}$ are concentrated in the upwelling regions, while flocs with $100 \mu\text{m} < D_i < 200 \mu\text{m}$ are concentrated in the downwelling regions (Figures 2d and 2e). In contrast, higher value region of $\mathcal{R}_A > 1$ (e.g., when D_i and D_j are both larger than $300 \mu\text{m}$) suggests the aggregation rates between two flocs smaller than $90 \mu\text{m}$ as well as those between flocs larger than $300 \mu\text{m}$ are enhanced by turbulence. This is because these flocs have similar spatial distributions in the water column, indicating

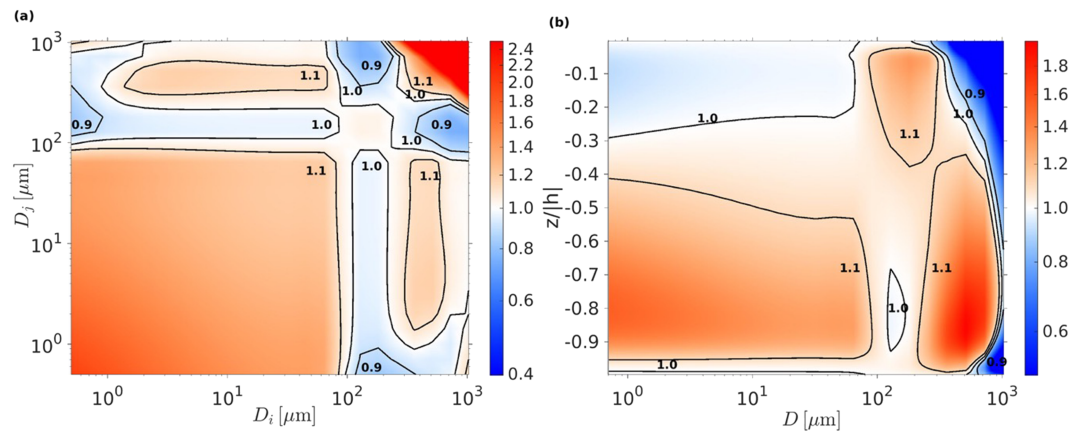


Figure 7. Turbulence effects on (a) aggregation rate (R_A) and (b) breakup rate (R_B) in Case BM. Labels of contour are shown in black. The horizontal (D_i) and vertical (D_j) axis in panel (a) are the diameter of two flocs that aggregate, respectively. The horizontal (D) in panel (b) is the diameter of flocs that break up, and vertical axis is the depth normalized by $|h|$.

the strongly positive correlation between the concentration of these flocs. This suggests turbulence plays a complicated role in aggregation: it enhances the aggregation rate of some flocs while it suppresses the aggregation rate of other flocs. The value of R_A suggests the bias in aggregation rate due to the use of horizontally averaged mass concentration and dissipation rate from the regional model without resolving three-dimensional nonhomogeneous turbulence (represented by the denominator) (e.g., COAWST, see Sherwood et al., 2018), compared to that due to the use of the mass concentration and dissipation rate diagnosed through turbulence-resolving model (represented by the numerator).

In order to quantify the turbulence effect on breakup rate, we define the ratio of breakup rate R_B :

$$R_B = \frac{\langle FP \rangle}{\langle F \rangle \langle P \rangle} = \frac{\langle CP \rangle}{\langle C \rangle \langle P \rangle}, \quad (20)$$

where the numerator is the breakup rate estimated by instantaneous floc mass concentration and dissipation rate and the denominator is the breakup rate estimated by horizontally averaged floc mass concentration and dissipation rate.

Contour of R_B at equilibrium with floc size in Case BM is shown in Figure 7b. The region of $R_B < 1$ (e.g., when $D > 700 \mu\text{m}$ and $z/|h| > -0.3$, where D is the diameter of flocs that break up) suggests that the breakup rate is suppressed by turbulence. This is mainly because the regions of higher floc mass concentration within the given size range are not at the same spatial locations as those of high dissipation rate. For instance, flocs with $D_i > 700 \mu\text{m}$ are concentrated in the midregion (Figure 4a), while dissipation rate is higher near the surface and seabed (Figure 1b). In contrast, higher value region of $R_B > 1$ (e.g., when $100 \mu\text{m} < D_i < 200 \mu\text{m}$, and $z/|h| > -0.1$) suggests the breakup rates of flocs of $100 \mu\text{m} < D_i < 200 \mu\text{m}$ are enhanced by turbulence close to the surface. This is because those flocs have higher concentration in the downwelling region with high dissipation rates. In the benchmark case, the turbulence alters aggregation rate by 20% to 98% for flocs of $D \leq 64.0 \mu\text{m}$. Although R_A is much larger than 1 for flocs larger than $700 \mu\text{m}$, the mass concentrations for flocs of those sizes are small. However, we are not able to derive formulas for R_A and R_B based on one simulation. More simulations, under different wind and wave conditions, are needed to quantify the effect of turbulence on aggregation and breakup rates.

4. Numerical Experiments and Discussion

A series of simulations (Cases B2-S4, see Table 1) are conducted to investigate the effects of forcing conditions, including wave breaking, wave forcing, and erosion fluxes, and particle properties including settling velocities on the flocculation processes and floc distribution.

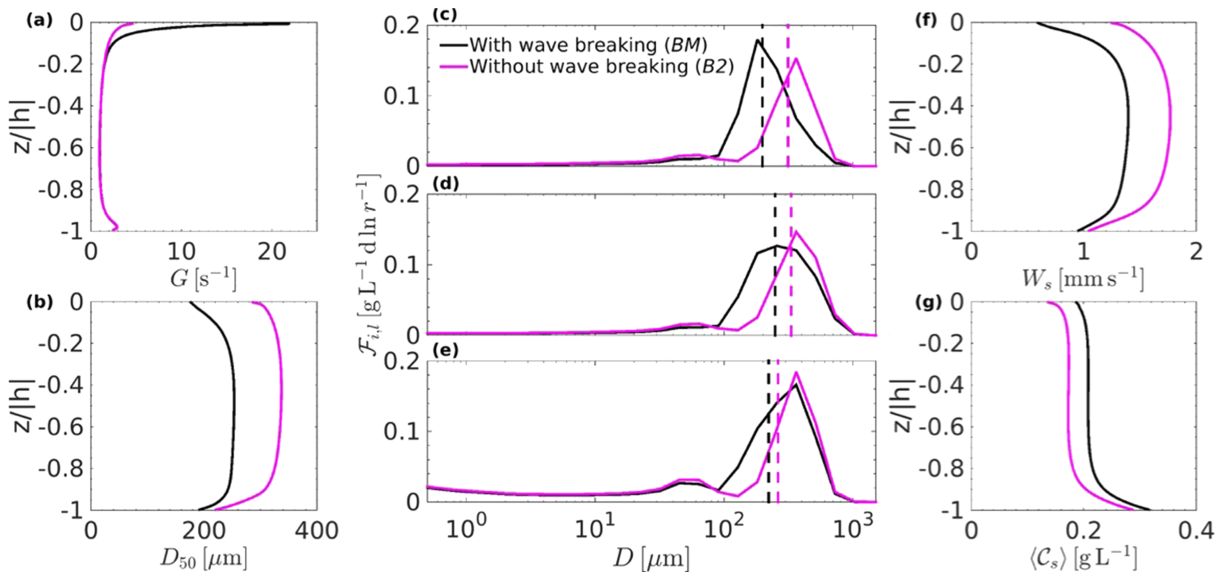


Figure 8. Profiles of (a) shear rate (G [s⁻¹]), (b) median floc size (D_{50} [μm]), (f) mass weighted settling velocity (W_s [mm s⁻¹]) and (g) total floc mass concentration ($\langle C_s \rangle$ [g L⁻¹]), with wave breaking (Case BM, black) and without wave breaking (Case B2, magenta). Floc size distribution (F_{il} [$\text{g L}^{-1} \text{dln} r^{-1}$], where l denotes layer average) averaged over: (c) near-surface region ($z/|h| > -0.1$), (d) midregion ($-0.9 \leq z/|h| \leq -0.1$), and (e) near-seabed region ($z/|h| < -0.9$) with wave breaking (Case BM, black) and without wave breaking (Case B2, magenta), respectively. Dashed lines indicate corresponding the median floc size (D_{50}) in each layer at the equilibrium.

4.1. Effects of Wave Breaking

In this section, we compare the simulation without wave breaking (Case B2) to the benchmark simulation with wave breaking (Case BM). The focus is on how wave breaking affects the FSD, floc mass concentration, and average settling velocity in the water column.

The comparison of the shear rate (G) between with wave breaking (Case BM) and without wave breaking (Case B2) is presented in Figure 8a. Near the surface, wave breaking greatly increases the shear rate, which is approximately one order of magnitude larger than that near the seabed. Away from the surface, shear rate is similar in both cases. Although the increase in shear rate due to wave breaking is only close to the surface, the resultant decrease in the median floc size (D_{50}) occurs throughout the water column (Figure 8b). The decrease in D_{50} due to wave breaking is the largest near the surface and is the smallest near the seabed.

The effects of wave breaking on the averaged FSDs in the near-surface region ($z/|h| > -0.1$), midregion ($-0.9 \leq z/|h| \leq -0.1$), and near-bed ($z/|h| < -0.9$) region are shown in Figures 8c–8e, respectively. With wave breaking, the peak of the FSD increases from near-surface region toward near-bed region, different from that without wave forcing (Figures 8c–8e). This suggests that the dominant floc size of the FSD changes with forcing conditions (e.g., with and without wave breaking). The change in forcing condition changes dissipation rate, vertical transport, and spatial distribution of flocs. Therefore, although there is inherent uncertainty in the parameters of flocculation model, it is necessary and helpful to couple size-resolving flocculation model in regional circulation model to investigate the suspended cohesive sediment transport under various hydrodynamic conditions in the nearshore, as recent attempt in Sherwood et al. (2018). In near-surface region, the enhanced shear rate leads to decrease in concentration of large flocs and increase in concentration of small flocs (Figure 8c). For instance, under the simulated condition, the floc mass concentration with wave breaking is more than five times greater than that without wave breaking for $D = 181.0 \mu\text{m}$, while it decreases due to wave breaking, by more than a half for $D = 362.0 \mu\text{m}$. The median floc size is the largest in the midregion (Figure 8d) due to low shear rate (Figure 8a) with and without the influence of wave breaking. In the near-bed region (Figure 8e), the major difference in floc mass is between $100 \mu\text{m}$ and $300 \mu\text{m}$, whereas there is little difference for larger flocs. The median floc size (D_{50}) is the largest near the seabed without wave breaking. In this case, equilibrium floc size is primarily controlled by the large concentration near the seabed (Figure 8f), since shear rate near the surface is similar to that near the seabed (Figure 8a).

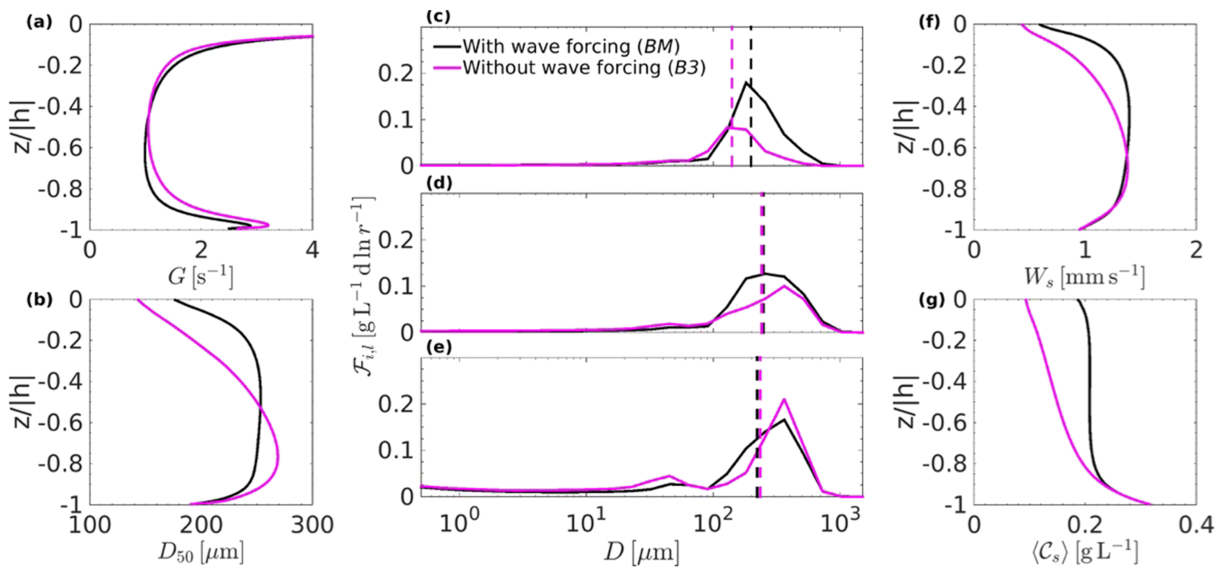


Figure 9. Profiles of (a) shear rate (G [s^{-1}]), (b) median floc size (D_{50} [μm]), (f) mass weighted settling velocity (W_s [mm s^{-1}]), and (g) total floc mass concentration (C_s [g L^{-1}]) with wave forcing (Case BM , black) and without wave forcing (Case $B3$, magenta). Floc size distribution (F_{il} [$\text{g L}^{-1} \text{d} \ln r^{-1}$], where l denotes layer average) averaged over: (c) near-surface region ($z/|h| > -0.1$), (d) midregion ($-0.9 \leq z/|h| \leq -0.1$), and (e) near-seabed region ($z/|h| < -0.9$) with wave forcing (Case BM , black) and without wave forcing (Case $B3$, magenta), respectively. Dashed lines indicate corresponding the median floc size (D_{50}) in each layer at the equilibrium.

In order to examine the effect of wave breaking on the settling velocity of total flocs, we here define the floc mass weighted settling velocity as follows:

$$W_s(z) = \sum_{j=1}^{N_b} w_{s,j} \frac{\langle C_j \rangle}{\langle C_s \rangle}, \quad (21)$$

where N_b is the total number of floc size bin. Similar to median floc size, W_s is the smallest near the surface (seabed) with (without) wave breaking. Wave breaking reduces the floc mass weighted settling velocity (W_s) in the whole water column (Figure 8f). This is because wave breaking reduces the number of larger flocs with faster settling velocity and increases the number of smaller flocs with slower settling velocity. Specifically, the difference in W_s between with wave breaking and without wave breaking is larger near the surface and decreases toward the seabed, respectively, under the simulated conditions.

Wave breaking increases the total floc mass concentration ($\langle C_s \rangle$ [g L^{-1}]) in the water column (Figures 8g) and reduces the vertical gradient in $\langle C_s \rangle$ near the surface compared to that without wave breaking. While horizontal currents are similar in cases with wave breaking (Case BM) and without wave breaking (Case $B2$), the increase in total floc mass concentration in the water column due to wave breaking (Figures 8f) also has important impact on the cross-shelf sediment transport. In order to quantify this effect, we calculate the cross-shelf sediment transport flux (\mathcal{T}_{cs} , in unit of $\text{kg m}^{-2} \text{s}^{-1}$) as follows:

$$\mathcal{T}_{cs} = \frac{1}{|h|} \int_h^0 \langle (u + u^{St}) C_s \rangle \text{ dz}. \quad (22)$$

Wave breaking increases the cross-shelf sediment transport by more than 15% compared to that without wave breaking under the simulated conditions.

4.2. Effects of Wave Forcing

In addition to wave-driven Langmuir turbulence, turbulence in continental shelf water can also arise purely from current shear, and has different characteristics from Langmuir turbulence. For instance, vertical velocity and mixing in shear turbulence (see Figures S2 and S3 in the supporting information for flow structure) is weaker and less coherent than that in Langmuir turbulence. Simulation $B3$ with the Stokes drift set to zero is conducted to investigate how turbulence type influences flocculation and floc distribution.

The comparison of the shear rate (G) between the simulation with (Case BM) and without wave forcing (Case $B3$) is shown in Figure 9a. Near the surface, G is similar for both cases. Away from the boundaries,

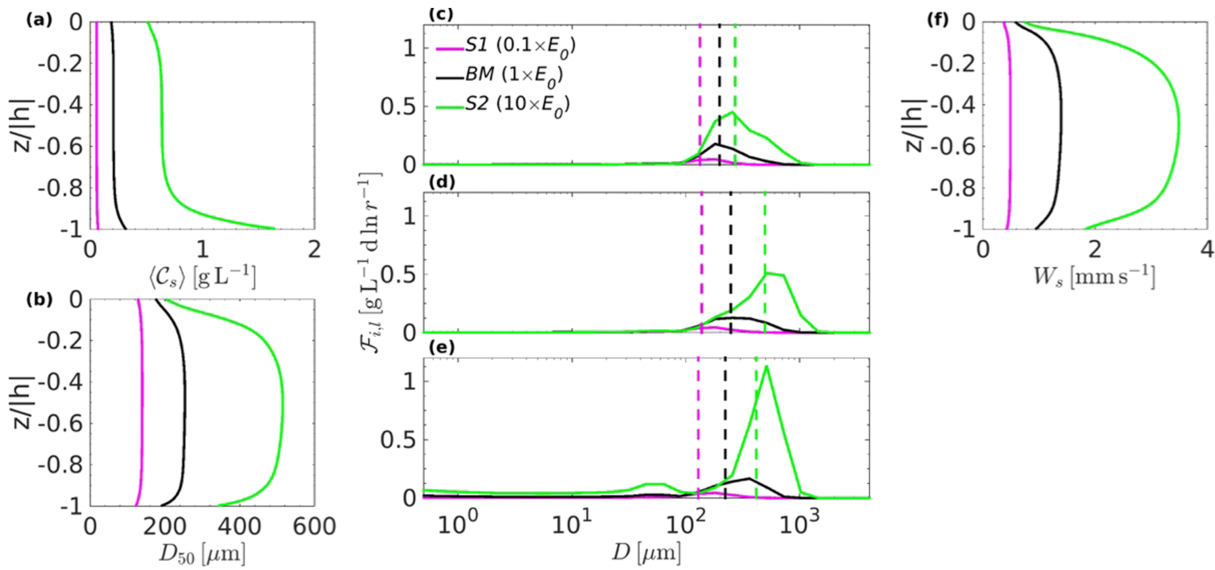


Figure 10. Profiles of (a) total floc mass concentration (C_s [g L⁻¹]), (b) median floc size (D_{50} [μm]), and (f) mass weighted settling velocity (W_s [mm s⁻¹]) in Case S1 ($0.1 \times E_0$, magenta), Case BM ($1.0 \times E_0$, black), and Case S2 ($10 \times E_0$, green), respectively. Floc size distribution ($\mathcal{F}_{l,l}$ [g L⁻¹ d ln r⁻¹], where l denotes layer average) averaged over: (c) near-surface region ($z/|h| > -0.1$), (d) midregion ($-0.9 \leq z/|h| \leq -0.1$), and (e) near-seabed region ($z/|h| < -0.9$) in Case S1 ($0.1 \times E_0$, magenta), Case BM ($1.0 \times E_0$, black), and Case S2 ($10 \times E_0$, green), respectively. Dashed lines indicate corresponding the median floc size (D_{50}) in each layer at the equilibrium.

wave forcing slightly increases G in the upper half of the water column, and decreases G in the lower half of the water column. The median floc size (D_{50}) without wave forcing is smaller than that with wave forcing in the upper half of the water column, and is larger in the lower half of the water column (Figure 9b). It is more uniform in the midregion with wave forcing compared to that without wave forcing, suggesting that wave-driven Langmuir turbulence enhances vertical mixing and transport of suspended sediments.

The effects of wave forcing on the averaged FSDs over the near-surface region, midregion, and near-bed region are shown in Figures 9c–9e, respectively. In near-surface region, the increase in the number of flocs that are brought up by the upwelling branch of Langmuir circulation leads to faster aggregation, and thus, increase in large flocs as shear rate is similar for both cases (Figures 9c). The difference in the mass concentration mainly occurs between 150 μm and 700 μm. In the midregion (Figures 9d), the peak size of the FSD with wave forcing is smaller than that without wave forcing, and wave forcing increases the mass concentration mainly between 100 μm and 600 μm. In the near-bed region (Figures 9e), wave forcing increases the mass concentration for 100 μm < D < 270 μm, but decreases that for 300 μm < D < 700 μm. The peak size of the FSD without wave forcing is the same as that with wave forcing near the seabed.

Wave forcing increases the mass weighted settling velocity above $z/|h| = -0.6$ (Figure 9f). Wave forcing also increases total amount of flocs in the water column (Figure 9g). The cross-shelf sediment transport with Langmuir turbulence is more than 15% larger than that without Langmuir turbulence under the simulated conditions.

4.3. Effects of Erosion Fluxes

Erosion is parameterized using equation (16) in simulation BM. It affects flocculation processes by changing the mass concentration of flocs in the water column. To test model sensitivity to the parameterization, we conduct additional experiments by decreasing/increasing the erodibility by a factor of 10 in Cases S1 and S2, respectively.

Increase in erosion fluxes leads to increase in both total floc mass concentration (Figures 10a) in the whole water column as expected. The increase in total floc mass concentration means the increase in the probability of floc collision and median floc size (Figures 10b), consistent with previous studies (e.g., Sherwood et al., 2018; Winterwerp, 1998). Therefore, D_{50} in simulation S2 is the largest, and D_{50} in simulation S1 is the smallest.

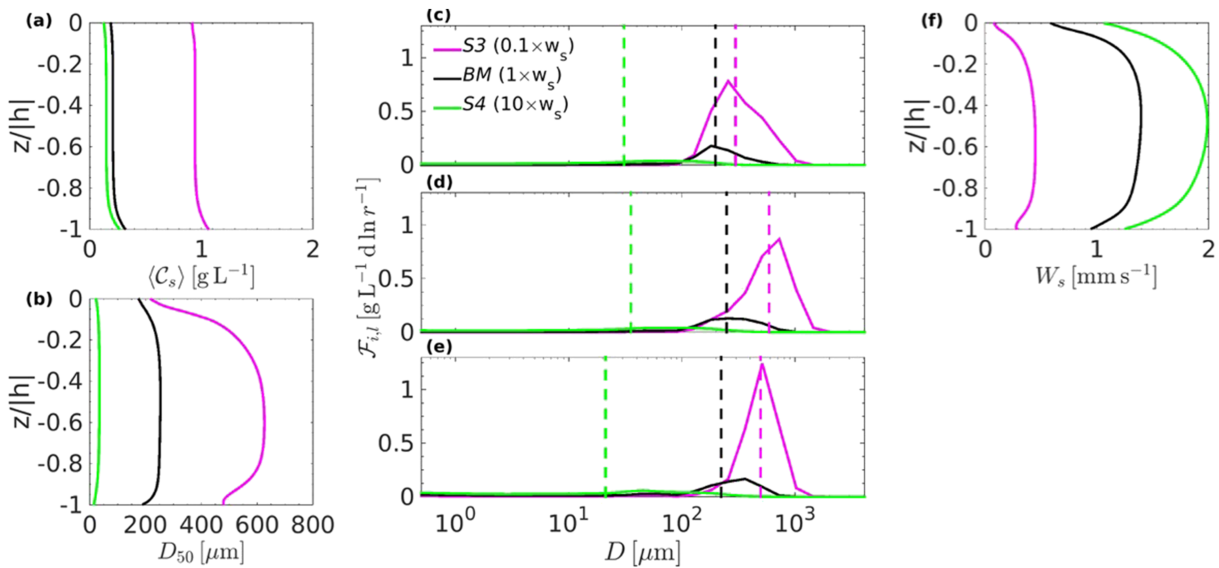


Figure 11. Profiles of (a) total floc mass concentration (C_s [g L^{-1}]), (b) median floc size (D_{50} [μm]), and (f) mass weighted settling velocity (W_s [mm s^{-1}]) in Case S3 ($0.1 \times w_s$, magenta), Case BM ($1.0 \times w_s$, black), and Case S4 ($10 \times w_s$, green), respectively. Floc size distribution ($\mathcal{F}_{i,l}$ [$\text{g L}^{-1} \text{d} \ln r^{-1}$], where l denotes layer average) averaged over: (c) near-surface region ($z/|h| > -0.1$), (d) midregion ($-0.9 \leq z/|h| \leq -0.1$), and (e) near-seabed region ($z/|h| < -0.9$) in Case S3 ($0.1 \times w_s$, magenta), Case BM ($1.0 \times w_s$, black), and Case S4 ($10 \times w_s$, green), respectively. Dashed lines indicate corresponding the median floc size (D_{50}) in each layer at the equilibrium.

The variations of averaged FSDs over the near-surface region, midregion, and near-bed region due to erosion fluxes are shown in Figures 10c–10e, respectively. The peak of the FSD moves toward larger size as erosion flux increases (Figures 10c–10e). In addition, increase in erosion fluxes increases the mass weighted settling velocity in the whole water column, with the largest increase in midregion and the smallest increase in near-surface region (Figure 10f). The cross-shelf sediment transport in Cases S1 and S2 are about 30% and 320% of that in Case BM under the simulated conditions, respectively. Considering that the increase/decrease in the erosion fluxes compared to the benchmark case is scaled by a factor of 10, the cross-shelf sediment transport due to presence of flocculation processes increases/decreases approximately by a factor of 3, which is disproportionate to the change in the erosion fluxes.

4.4. Effects of Settling Velocities

Settling velocity is parameterized using equation (9) based on in situ observation (Sternberg et al., 1999). There are a number of other formulas for settling velocity (e.g., Khelifa & Hill, 2006; Strom & Keyvani, 2011; Winterwerp, 2002). To test the sensitivity test of model results to w_s , we conduct additional experiments by decreasing/increasing settling velocities by a factor of 10 in Cases S3 and S4, respectively.

Increase in settling velocities of the flocs reduces the total amount of flocs in the water column (Figure 11a) due to reduced residence time. The decrease in total floc mass concentration means the decrease in the probability of floc collision and median floc size (Figure 11b). The median floc size in simulation S4 is more nonuniform than that in simulation S3. The variations of averaged FSDs over the near-surface region, midregion, and near-bed region due to erosion fluxes are shown in Figures 11c–11e, respectively. The peak of the FSD moves toward larger size as settling velocity decreases. In addition, increase in settling velocity of flocs in individual size bin increases the mass weighted settling velocity in the whole water column (Figures 11f). The cross-shelf sediment transport in Cases S3 and S4 are about 440% and 70% of that in Case BM under the simulated conditions, respectively.

As total SSC once equilibrium is reached is dependent on the settling velocity and erosion flux, increase in the settling velocity decreases the total floc mass concentration and median floc size, which is similar to the effect when erosion flux decreases.

5. Conclusions

In this study, we use a LES model to investigate the effect of flocculation processes on suspended cohesive sediment in Langmuir turbulence. We also examine the impact of Langmuir turbulence on flocculation processes. The analysis was conducted by examining instantaneous snapshots of flow and floc mass concentration, and the mean, the variance, and the skewness of floc mass concentration. Sensitivity tests were performed to examine how different turbulence type and sediment properties influence flocculation processes. The major conclusions of this study are as follows:

1. Wave breaking is more important for cohesive sediment transport than the noncohesive sediment in the coastal ocean. Although wave breaking influences dynamics close to the ocean surface, it affects floc distribution in the whole water column. It increases the total floc mass concentration in the water column, by reducing the median floc size and averaged settling velocity. The cross-shelf sediment transport ($\sim 0.055 \text{ kg m}^{-2} \text{ s}^{-1}$) with wave breaking is more than 15% larger than that without wave breaking under the simulated conditions.
2. In Langmuir turbulence, both turbulent shear rate and flocs are nonuniformly distributed. Consequently, flocs experience aggregation and breakup at the rates either enhanced or suppressed by the nonhomogeneous turbulence. The modulated flocculation processes result in FSD that changes with depth, and floc mass concentration profile that varies with floc size. Therefore, the FSD at a certain depth in Langmuir turbulence is not representative of the water column.
3. Langmuir turbulence increases the total floc mass concentration in the water column, compared to shear turbulence. It also increases the cross-shelf sediment transport by more than 15% compared to shear turbulence under the simulated conditions, which is comparable to that due to wave breaking.
4. Flocculation processes and the FSDs are also sensitive to bed erosion and floc properties including settling velocity. Large settling velocity, strong turbulence, and low bed erosion rate are favorable conditions for small median floc size, while small settling velocity and high bed erosion rate are favorable conditions for high suspended floc concentration.

The results in this study highlight the importance of full-depth wave-driven Langmuir turbulence and flocculation processes in the horizontal transport and vertical distribution of cohesive sediment in the coastal ocean, and could have the following implications. First, Langmuir cells that span the whole water column under favorable wind and wave conditions in shallow seas (e.g., Gargett et al., 2004) enhance cross-shelf sediment transport by increasing the amount of suspended sediment. Parameterization for Langmuir turbulence should be included in any regional sediment transport studies. Second, the results also suggest that floc size changes with meteorological conditions. Prescribed settling velocity that is a common practice in coastal sediment models is inaccurate for regions with cohesive seabed such as the northern Gulf of Mexico (e.g., Safak et al., 2013; Bentley et al., 2016) because of variable meteorological and wave conditions. The use of flocculation model in coastal sediment models (e.g., Sherwood et al., 2018) will likely improve the prediction of sediment transport in those regions.

There are a number of future directions that require collaboration between the observational and the modeling community. For example, the bottom boundary layer is not resolved in this study. When it is resolved, sediment-induced stratification becomes a substantial sink of turbulence kinetic energy (e.g., Ozdemir et al., 2010; Yu et al., 2013) and may modulate flocculation processes and sediment distribution. The bottom boundary condition can be improved following Schulz and Umlauf (2016) to alleviate the dependence of deposition flux for large particles on the resolution of the lowermost grid. Model realism can also be improved by adding a bed model so that mud consolidation, swelling, and the dynamic evolution of bed source (e.g., Sanford, 2008; Shen et al., 2018a; Sherwood et al., 2018; Warner et al., 2008) are included. Finally, laboratory experiments and field observations on floc evolution in three-dimensional nonhomogenous turbulence environment (e.g., Langmuir turbulence in coastal oceans) are currently lacking but are critical to better constrain coupled-turbulence-flocculation model and to improve our understanding of flocculation processes in turbulent flows in natural environments.

Appendix A: Validation of Flocculation Model

Here we evaluated the flocculation model by comparing with results from the laboratory experiments in a settling column (Winterwerp, 1998) and a turbulent mixing tank (Tran et al., 2018), respectively. The initial

particle size is assumed to be equal to the size of the primary particles in each experiment. The offline 0D flocculation model (i.e., only the four terms on RHS of equation (3) are retained) is run until the FSD reaches steady state. The results are summarized in Table A1 and Figure A1. The model results agree fairly well with the laboratory data of both Winterwerp (1998) and Tran et al. (2018).

Table A1
Parameters in Measured and Modeled Results From the Laboratory Experiments by Winterwerp (1998) (With Label T) and Tran et al. (2018) (With Label NPS)

Case	C_0 (g L ⁻¹)	G(s ⁻¹)	D_{50} measured (μm)	D_{50} modeled (μm)
NPS1	0.1	50	117	113
NPS2	0.2	50	121	125
NPS3	0.4	50	145	142
T71	0.65	7.3	270	358
T69	1.17	28.9	241	202
T73	1.21	81.7	140	125

Table A2
A Table of Parameters Used in Flocculation Model

Symbol	Description	Value	Unit
D_p	Diameter of primary particle	0.5	m
F_y	Floc yield strength	10^{-10}	N
N_f	Fractal dimension	2.0	unitless
A_1, A_2, A_3, A_4, A_5 , and $\alpha_{1,1}$	Tunable aggregation parameters	0.02, 0.4, 3, 55, 0.18, and 0.95, respectively	unitless
\mathcal{E}, C_1 , and C_2	Tunable breakup parameters	3.0×10^{-7} , 0.5, and 1.0, respectively	unitless
μ	Dynamic viscosity	10^{-3}	kg m ⁻¹ s ⁻¹
ν	Kinematic viscosity	10^{-6}	m ² s ⁻¹
ρ_s	Density of primary particles	2650	kg m ⁻³

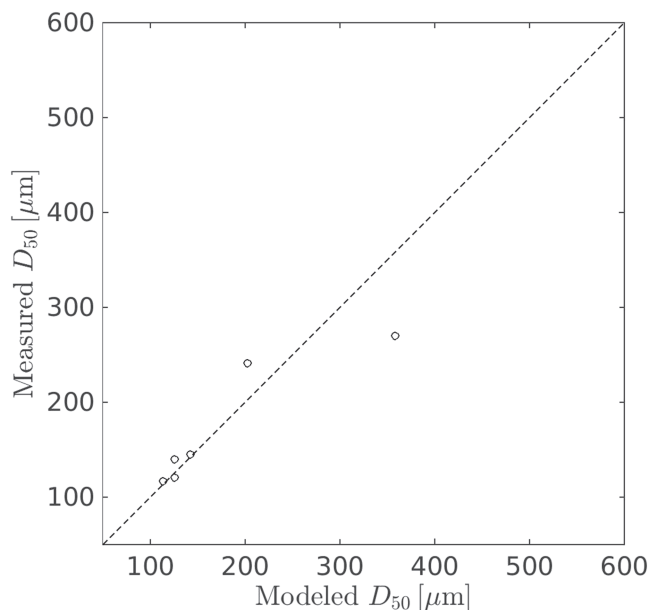


Figure A1. Comparison of median floc size between measured and modeled results.

Acknowledgments

We greatly appreciate Dr. Fanghua Xu who generously shared the MATLAB and Fortran scripts to generate the figures in Xu et al. (2008) for comparison of 0-D flocculation model. The authors acknowledge support from the National Key Research Program of China (2017YFA0604100). J. L., J. H. L., and Q. C. were funded by the National Science Foundation (CCF-153956). J. L. and J. H. L. were also funded by NSF through Grant OCE-1521018 and a grant from the Gulf of Mexico Research Initiative. C. E. O. was funded by the Louisiana Board of Regents through Research Competitiveness Subprogram (contract ID: 127-15-4131). K. X. was funded by Louisiana Center of Excellence (Award CPRA-2015-COE-JE) as well as NSF Coastal SEES Program (Award 1427389). Computation was performed using supercomputers at Louisiana State University, at Louisiana Optical Network Infrastructure (LONI), and at the National Center for Atmospheric Research. Numerical solutions used for the plots are publicly available through the Gulf of Mexico Research Initiative Information and Data Cooperative (<https://data.gulfresearchinitiative.org/pelagos-symfony/data/R6.x819.000:0002>, DOI:10.7266/n7-k9hq-hr97).

References

- Ariathurai, R., & Arulanandan, K. (1978). Erosion rates of cohesive soils. *Journal of the Hydraulics Division*, 104(2), 279–283.
- Bäbler, M. U., Sefcik, J., Morbidelli, M., & Baldyga, J. (2006). Hydrodynamic interactions and orthokinetic collisions of porous aggregates in the Stokes regime. *Physics of Fluids*, 18(1), 13302.
- Bannister, R., Battershill, C., & De Nys, R. (2012). Suspended sediment grain size and mineralogy across the continental shelf of the great barrier reef: Impacts on the physiology of a coral reef sponge. *Continental Shelf Research*, 32, 86–95.
- Benson, T., & French, J. (2007). Insipid: A new low-cost instrument for in situ particle size measurements in estuarine and coastal waters. *Journal of Sea Research*, 58(3), 167–188.
- Bentley, S. Sr., Blum, M., Maloney, J., Pond, L., & Paulsell, R. (2016). The Mississippi River source-to-sink system: Perspectives on tectonic, climatic, and anthropogenic influences, miocene to anthropocene. *Earth-Science Reviews*, 153, 139–174.
- Berry, E. X. (1967). Cloud droplet growth by collection. *Journal of the Atmospheric Sciences*, 24(6), 688–701.
- Braithwaite, K., Bowers, D., Nimmo Smith, W., & Graham, G. (2012). Controls on floc growth in an energetic tidal channel. *Journal of Geophysical Research*, 117, C02024. <https://doi.org/10.1029/2011JC007094>
- Brunner, K., Kukulka, T., Proskurowski, G., & Law, K. (2015). Passive buoyant tracers in the ocean surface boundary layer: 2. observations and simulations of microplastic marine debris. *Journal of Geophysical Research: Oceans*, 120, 7559–7573. <https://doi.org/10.1002/2015JC010840>
- Burd, A., & Jackson, G. (1997). Predicting particle coagulation and sedimentation rates for a pulsed input. *Journal of Geophysical Research*, 102(C5), 10,545–10,561.
- Burd, A. B., & Jackson, G. A. (2009). Particle aggregation. *Annual Review of Marine Science*, 1, 65–90. <https://doi.org/10.1146/annurev.marine.010908.163904>
- Chamecki, M., Meneveau, C., & Parlange, M. B. (2008). A hybrid spectral/finite-volume algorithm for large-eddy simulation of scalars in the atmospheric boundary layer. *Boundary-Layer Meteorology*, 128(3), 473–484.
- Chen, S.-N., Geyer, W. R., Sherwood, C. R., & Ralston, D. K. (2010). Sediment transport and deposition on a river-dominated tidal flat: An idealized model study. *Journal of Geophysical Research*, 115, C10040. <https://doi.org/10.1029/2010JC006248>
- D'Asaro, E. A. (2014). Turbulence in the upper-ocean mixed layer. *Annual Review of Marine Science*, 6, 101–115. <https://doi.org/10.1146/annurev-marine-010213-135138>
- D'Sa, E. J., Joshi, I., & Liu, B. (2018). Galveston bay and coastal ocean optical-geochemical response to hurricane harvey from viirs ocean color. *Geophysical Research Letters*, 45, 10,579–10,589. <https://doi.org/10.1029/2018GL079954>
- Davis, R. A. (2017). Sediments of the gulf of mexico. In *Habitats and Biota of the Gulf of Mexico: Before the Deepwater Horizon Oil Spill*, (pp. 165–215). Springer.
- Dierssen, H., Zimmerman, R. C., Drake, L. A., & Burdige, D. J. (2009). Potential export of unattached benthic macroalgae to the deep sea through wind-driven langmuir circulation. *Geophysical Research Letters*, 36 L04602. <https://doi.org/10.1029/2008GL036188>
- Dietrich, W. E. (1982). Settling velocity of natural particles. *Water Resources Research*, 18(6), 1615–1626.
- Droppo, I., Leppard, G., Liss, S., & Milligan, T., (2004). Flocculation in natural and engineered environmental systems. *Flocculation in natural and engineered environmental systems*.
- Droppo, I., Walling, D., & Ongley, E. (1998). Suspended sediment structure: implications for sediment and contaminant transport modelling. *IAHS-AISH Publication*, 437–444.
- Droppo, I. G. (2006). Suspended sediment transport–flocculation and particle characteristics. *Encyclopedia of Hydrological Sciences*.
- Drucker, R., Martin, S., & Moritz, R. (2003). Observations of ice thickness and frazil ice in the st. lawrence island polynya from satellite imagery, upward looking sonar, and salinity/temperature moorings. *Journal of Geophysical Research*, 108(C5), 3149. <https://doi.org/10.1029/2001JC001213>
- Dyer, K. (1989). Sediment processes in estuaries: future research requirements. *Journal of Geophysical Research*, 94(C10), 14,327–14,339.
- Eisma, D., & Li, A. (1993). Changes in suspended-matter floc size during the tidal cycle in the dollard estuary. *Netherlands Journal of Sea Research*, 2.
- Fan, Y., Jarosz, E., Yu, Z., Rogers, W., Jensen, T., & Liang, J.-H. (2018). Langmuir turbulence in horizontal salinity gradient. *Ocean Modelling*, 129, 93–103.
- Ferguson, R., & Church, M. (2004). A simple universal equation for grain settling velocity. *Journal of Sedimentary Research*, 74(6), 933–937.
- Gargett, A., Wells, J., Tejada-Martinez, A., & Grosch, C. (2004). Langmuir supercells: A mechanism for sediment resuspension and transport in shallow seas. *Science*, 306(5703), 1925–1928. <https://doi.org/10.1126/science.1100849>
- Gargett, A. E., & Wells, J. R. (2007). Langmuir turbulence in shallow water. part 1. observations. *Journal of Fluid Mechanics*, 576, 27–61.
- Gaskell, P., & Lau, A. (1988). Curvature-compensated convective transport: Smart, a new boundedness-preserving transport algorithm. *International Journal for Numerical Methods in Fluids*, 8(6), 617–641.
- Geyer, W., Hill, P., & Kineke, G. (2004). The transport, transformation and dispersal of sediment by buoyant coastal flows. *Continental Shelf Research*, 24(7–8), 927–949.
- Grosch, C., & Gargett, A. (2016). Why do less of langmuir supercells not include rotation? *Journal of Physical Oceanography*, 46(12), 3595–3597.
- Hamilton, P. E., Van Roekel, L. P., Fox-Kemper, B., Julien, K., & Chini, G. P. (2014). Langmuir–submesoscale interactions: Descriptive analysis of multiscale frontal spindown simulations. *Journal of Physical Oceanography*, 44(9), 2249–2272.
- Harcourt, R. R. (2015). An improved second-moment closure model of langmuir turbulence. *Journal of Physical Oceanography*, 45(1), 84–103.
- Harris, C. K., Traykovski, P. A., & Geyer, W. R. (2005). Flood dispersal and deposition by near-bed gravitational sediment flows and oceanographic transport: A numerical modeling study of the eel river shelf, northern California. *Journal of Geophysical Research*, 110, C09025. <https://doi.org/10.1029/2004JC002727>
- Harris, C. K., & Wiberg, P. (2002). Across-shelf sediment transport: Interactions between suspended sediment and bed sediment. *Journal of Geophysical Research*, 107(C1), 3008. <https://doi.org/10.1029/2000JC000634>
- Hill, P. S., Syvitski, J. P., Cowan, E. A., & Powell, R. D. (1998). In situ observations of floc settling velocities in glacier bay, alaska. *Marine Geology*, 145(1–2), 85–94.
- Hill, P. S., Voulgaris, G., & Trowbridge, J. H. (2001). Controls on floc size in a continental shelf bottom boundary layer. *Journal of Geophysical Research*, 106(C5), 9543–9549.
- Jackson, G. A., & Burd, A. B. (2015). Simulating aggregate dynamics in ocean biogeochemical models. *Progress in Oceanography*, 133, 55–65.
- Janin, J., Lepoint, F., & Pechon, P. (1992). Telemac-3d: A finite element code to solve 3d free surface flow problems. In *Computer modelling of seas and coastal regions* (pp. 489–506). Springer.

- Keyvani, A., & Strom, K. (2014). Influence of cycles of high and low turbulent shear on the growth rate and equilibrium size of mud flocs. *Marine Geology*, 354, 1–14.
- Khelifa, A., & Hill, P. S. (2006). Models for effective density and settling velocity of flocs. *Journal of Hydraulic Research*, 44(3), 390–401.
- Kolmogorov, A. N. (1941). The local structure of turbulence in incompressible viscous fluid for very large reynolds numbers. *Doklady Akademii Nauk SSSR*, 30, 301–305.
- Kranenburg, C. (1994). The fractal structure of cohesive sediment aggregates. *Estuarine, Coastal and Shelf Science*, 39(5), 451–460.
- Kukulka, T., Plueddemann, A. J., & Sullivan, P. P. (2012). Nonlocal transport due to langmuir circulation in a coastal ocean. *Journal of Geophysical Research*, 117 C12007. <https://doi.org/10.1029/2012JC008340>
- Kuprenas, R., Tran, D., & Strom, K. (2018). A shear-limited flocculation model for dynamically predicting average floc size. *Journal of Geophysical Research: Oceans*, 123, 6736–6752. <https://doi.org/10.1029/2018JC014154>
- Kusters, K. A. (1991). The influence of turbulence on aggregation of small particles in agitated vessels (ph. d. thesis).
- Law, B. A., Hill, P., Milligan, T., Curran, K., Wiberg, P., & Wheatcroft, R. (2008). Size sorting of fine-grained sediments during erosion: results from the western gulf of lions. *Continental Shelf Research*, 28(15), 1935–1946.
- Lee, B. J., Fettweis, M., Toorman, E., & Molz, F. J. (2012). Multimodality of a particle size distribution of cohesive suspended particulate matters in a coastal zone. *Journal of Geophysical Research*, 117, C03014. <https://doi.org/10.1029/2011JC007552>
- Lee, B. J., Toorman, E., Molz, F. J., & Wang, J. (2011). A two-class population balance equation yielding bimodal flocculation of marine or estuarine sediments. *Water Research*, 45(5), 2131–2145. <https://doi.org/10.1016/j.watres.2010.12.028>
- Leibovich, S. (1983). The form and dynamics of langmuir circulations. *Annual Review of Fluid Mechanics*, 15(1), 391–427.
- Lentz, S. J., & Fewings, M. R. (2012). The wind-and-wave-driven inner-shelf circulation. *Annual Review of Marine Science*, 4, 317–343. <https://doi.org/10.1146/annurev-marine-120709-142745>
- Liang, J.-H., Deutsch, C. A., McWilliams, J. C., Baschek, B., Sullivan, P. P., & Chiba, D. (2013). Parameterizing bubble-mediated air-sea gas exchange and its effect on ocean ventilation. *Global Biogeochemical Cycles*, 27, 894–905. <https://doi.org/10.1002/gbc.20080>
- Liang, J.-H., Emerson, S. R., D'Asaro, E. A., McNeil, C. L., Harcourt, R. R., Sullivan, P. P., et al. (2017). On the role of sea-state in bubble-mediated air-sea gas flux during a winter storm. *Journal of Geophysical Research: Oceans*, 122, 2671–2685. <https://doi.org/10.1002/2016JC012408>
- Liang, J.-H., McWilliams, J. C., Sullivan, P. P., & Baschek, B. (2011). Modeling bubbles and dissolved gases in the ocean. *Journal of Geophysical Research*, 116(C3), C03015. <https://doi.org/10.1029/2010JC006579>
- Liang, J.-H., McWilliams, J. C., Sullivan, P. P., & Baschek, B. (2012). Large eddy simulation of the bubbly ocean: New insights on subsurface bubble distribution and bubble-mediated gas transfer. *Journal of Geophysical Research*, 117(C4), C04002. <https://doi.org/10.1029/2011JC007766>
- Liang, J.-H., Wan, X., Rose, K. A., Sullivan, P. P., & McWilliams, J. C. (2018). Horizontal dispersion of buoyant materials in the ocean surface boundary layer. *Journal of Physical Oceanography*, 48(9), 2103–2125. <https://doi.org/10.1175/JPO-D-18-0020.1>
- Lick, W., Huang, H., & Jepsen, R. (1993). Flocculation of fine-grained sediments due to differential settling. *Journal of Geophysical Research*, 98(C6), 10,279–10,288.
- Liu, J., Liang, J.-H., McWilliams, J. C., Sullivan, P. P., Fan, Y., & Chen, Q. (2018). Effect of planetary rotation on oceanic surface boundary layer turbulence. *Journal of Physical Oceanography*, 48(9), 2057–2080.
- Liu, W. T., Katsaros, K. B., & Businger, J. A. (1979). Bulk parameterization of air-sea exchanges of heat and water vapor including the molecular constraints at the interface. *Journal of the Atmospheric Sciences*, 36(9), 1722–1735.
- Maerz, J., Verney, R., Wirtz, K., & Feudel, U. (2011). Modeling flocculation processes: Intercomparison of a size class-based model and a distribution-based model. *Continental Shelf Research*, 31(10), S84–S93.
- Maerz, J., & Wirtz, K. (2009). Resolving physically and biologically driven suspended particulate matter dynamics in a tidal basin with a distribution-based model. *Estuarine, Coastal and Shelf Science*, 84(1), 128–138.
- Maggi, F. (2005). Flocculation dynamics of cohesive sediment.
- Maggi, F. (2007). Variable fractal dimension: A major control for floc structure and flocculation kinematics of suspended cohesive sediment. *Journal of Geophysical Research*, 112(C7), C07012. <https://doi.org/10.1029/2006JC003951>
- McCave, I. (1984). Size spectra and aggregation of suspended particles in the deep ocean. *Deep Sea Research Part A. Oceanographic Research Papers*, 31(4), 329–352.
- McWilliams, J. C., Huckle, E., Liang, J., & Sullivan, P. P. (2014). Langmuir turbulence in swell. *Journal of Physical Oceanography*, 44(3), 870–890. <https://doi.org/10.1175/JPO-D-13-0122.1>
- McWilliams, J. C., Huckle, E., Liang, J.-H., & Sullivan, P. P. (2012). The wavy ekman layer: Langmuir circulations, breaking waves, and reynolds stress. *Journal of Physical Oceanography*, 42(11), 1793–1816.
- McWilliams, J. C., Sullivan, P. P., & Moeng, C.-H. (1997). Langmuir turbulence in the ocean. *Journal of Fluid Mechanics*, 334, 1–30.
- Mehta, A. J. (2013). *An introduction to hydraulics of fine sediment transport*, (Vol. 38). World Scientific Publishing Company.
- Mietta, F., Chassagne, C., Manning, A. J., & Winterwerp, J. C. (2009). Influence of shear rate, organic matter content, ph and salinity on mud flocculation. *Ocean Dynamics*, 59(5), 751–763.
- Mikkelsen, O. A., Hill, P. S., & Milligan, T. G. (2007). Seasonal and spatial variation of floc size, settling velocity, and density on the inner adriatic shelf (italy). *Continental Shelf Research*, 27(3–4), 417–430.
- Moriarty, J. M., Harris, C. K., Friedrichs, M. A., Fennel, K., & Xu, K. (2018). Impact of seabed resuspension on oxygen and nitrogen dynamics in the northern gulf of mexico: A numerical modeling study. *Journal of Geophysical Research: Oceans*.
- Ogston, A., & Sternberg, R. (1999). Sediment-transport events on the northern california continental shelf. *Marine Geology*, 154(1–4), 69–82.
- Ouwensloot, H., Vilà-Guerau de Arellano, J., van Heerwaarden, C., Ganzeveld, L., Krol, M., & Lelieveld, J. (2011). On the segregation of chemical species in a clear boundary layer over heterogeneous land surfaces. *Atmospheric Chemistry and Physics*, 11(20), 10,681–10,704.
- Ozdemir, C. E., Hsu, T.-J., & Balachandar, S. (2010). A numerical investigation of fine particle laden flow in an oscillatory channel: the role of particle-induced density stratification. *Journal of Fluid Mechanics*, 665, 1–45.
- Passow, U., Zier vogel, K., Asper, V., & Diercks, A. (2012). Marine snow formation in the aftermath of the deepwater horizon oil spill in the gulf of mexico. *Environmental Research Letters*, 7(3), 035,301.
- Rubey, W. W. (1933). Settling velocity of gravel, sand, and silt particles. *American Journal of Science*, 148, 325–338.
- Safak, I., Allison, M., & Shermert, A. (2013). Floc variability under changing turbulent stresses and sediment availability on a wave energetic muddy shelf. *Continental Shelf Research*, 53, 1–10.
- Sanford, L. P. (2008). Modeling a dynamically varying mixed sediment bed with erosion, deposition, bioturbation, consolidation, and armoring. *Computers & Geosciences*, 34(10), 1263–1283.
- Sanford, L. P., & Halka, J. P. (1993). Assessing the paradigm of mutually exclusive erosion and deposition of mud, with examples from upper Chesapeake Bay. *Marine Geology*, 114(1–2), 37–57.

- Schulz, K., & Umlauf, L. (2016). Residual transport of suspended material by tidal straining near sloping topography. *Journal of Physical Oceanography*, 46(7), 2083–2102.
- Schwab, W. C., Baldwin, W. E., Hapke, C. J., Lentz, E. E., Gayes, P. T., Denny, J. F., et al. (2013). Geologic evidence for onshore sediment transport from the inner continental shelf: Fire island, new york. *Journal of Coastal Research*, 29(3), 526–544.
- Shen, X., Lee, B. J., Fettweis, M., & Toorman, E. A. (2018). A tri-modal flocculation model coupled with telemac for estuarine muds both in the laboratory and in the field. *Water Research*, 145, 473–486. <https://doi.org/10.1016/j.watres.2018.08.062>
- Shen, X., & Maa, J. P.-Y. (2017). Floc size distributions of suspended kaolinite in an advection transport dominated tank: measurements and modeling. *Ocean Dynamics*, 67(11), 1495–1510.
- Shen, X., Toorman, E. A., Lee, B. J., & Fettweis, M. (2018). Biophysical flocculation of suspended particulate matters in belgian coastal zones. *Journal of Hydrology*, 567, 238–252.
- Sherwood, C. R., Aretxabaleta, A. L., Harris, C. K., Rinehimer, J. P., Verney, R., & Ferré, B. (2018). Cohesive and mixed sediment in the regional ocean modeling system (roms v3. 6) implemented in the coupled ocean-atmosphere-wave-sediment transport modeling system (coawst r1234). *Geoscientific Model Development*, 11(5), 1849–1871.
- Shrestha, K., Anderson, W., & Kuehl, J. (2018). Langmuir turbulence in coastal zones: structure and length scales. *Journal of Physical Oceanography*, 48(5), 1089–1115.
- Shrestha, P. L., & Blumberg, A. F. (2005). Cohesive sediment transport. *Encyclopedia of Coastal Science*, 327–330.
- Smith, K. M., Hamlington, P. E., & Fox-Kemper, B. (2016). Effects of submesoscale turbulence on ocean tracers. *Journal of Geophysical Research: Oceans*, 121, 908–933. <https://doi.org/10.1002/2015JC011089>
- Son, M., & Hsu, T.-J. (2009). The effect of variable yield strength and variable fractal dimension on flocculation of cohesive sediment. *Water Research*, 43(14), 3582–3592. <https://doi.org/10.1016/j.watres.2009.05.016>
- Son, M., & Hsu, T.-J. (2011). The effects of flocculation and bed erosion on modeling cohesive sediment resuspension. *Journal of Geophysical Research*, 116, C03021. <https://doi.org/10.1029/2010JC006352>
- Soos, M., Wang, L., Fox, R., Sefcik, J., & Morbidelli, M. (2007). Population balance modeling of aggregation and breakage in turbulent taylor-couette flow. *Journal of Colloid and Interface Science*, 307(2), 433–446.
- Soulsby, R., & Whitehouse, R., (1997). Threshold of sediment motion in coastal environments. In *Pacific Coasts and Ports' 97: Proceedings of the 13th Australasian Coastal and Ocean Engineering Conference and the 6th Australasian Port and Harbour Conference*, (Vol. 1, pp. 145–150). Centre for Advanced Engineering, University of Canterbury.
- Spicer, P. T., & Pratsinis, S. E. (1996). Coagulation and fragmentation: Universal steady-state particle-size distribution. *AICHE Journal*, 42(6), 1612–1620.
- Sternberg, R., Berhane, I., & Ogston, A. (1999). Measurement of size and settling velocity of suspended aggregates on the northern california continental shelf. *Marine Geology*, 154(1–4), 43–53.
- Strom, K., & Keyvani, A. (2011). An explicit full-range settling velocity equation for mud flocs. *Journal of Sedimentary Research*, 81(12), 921–934.
- Strom, K., & Keyvani, A. (2016). Flocculation in a decaying shear field and its implications for mud removal in near-field river mouth discharges. *Journal of Geophysical Research: Oceans*, 121, 2142–2162. <https://doi.org/10.1002/2015JC011169>
- Sullivan, P. P., & McWilliams, J. C. (2010). Dynamics of winds and currents coupled to surface waves. *Annual Review of Fluid Mechanics*, 42, 19–42.
- Sullivan, P. P., McWILLIAMS, J. C., & Melville, W. K. (2007). Surface gravity wave effects in the oceanic boundary layer: Large-eddy simulation with vortex force and stochastic breakers. *Journal of Fluid Mechanics*, 593, 405–452.
- Sullivan, P. P., McWilliams, J. C., & Moeng, C.-H. (1994). A subgrid-scale model for large-eddy simulation of planetary boundary-layer flows. *Boundary-Layer Meteorology*, 71(3), 247–276.
- Sullivan, P. P., McWilliams, J. C., & Moeng, C.-H. (1996). A grid nesting method for large-eddy simulation of planetary boundary-layer flows. *Boundary-Layer Meteorology*, 80(1–2), 167–202.
- Sullivan, P. P., Romero, L., McWilliams, J. C., & Melville, W. K. (2012). Transient evolution of langmuir turbulence in ocean boundary layers driven by hurricane winds and waves. *Journal of Physical Oceanography*, 42(11), 1959–1980.
- Suzuki, N., & Fox-Kemper, B. (2016). Understanding stokes forces in the wave-averaged equations. *Journal of Geophysical Research: Oceans*, 121, 3579–3596.
- Tejada-Martinez, A., & Grosch, C. (2007). Langmuir turbulence in shallow water. part 2. large-eddy simulation. *Journal of Fluid Mechanics*, 576, 63–108.
- Terray, E., Donelan, M., Agrawal, Y., Drennan, W., Kahma, K., Williams, A. J., et al. (1996). Estimates of kinetic energy dissipation under breaking waves. *Journal of Physical Oceanography*, 26(5), 792–807.
- Thorpe, S. A. (2005). *The turbulent ocean*. Cambridge University Press.
- Tran, D., Kuprenas, R., & Strom, K. (2018). How do changes in suspended sediment concentration alone influence the size of mud flocs under steady turbulent shearing? *Continental Shelf Research*, 158, 1–14.
- van Leussen, W. (1994). Estuarine macroflocs and their role in fine-grained sediment transport, *Ph. D. Thesis, University of Utrecht*.
- Van Roeke, L., Fox-Kemper, B., Sullivan, P., Hamlington, P., & Haney, S. (2012). The form and orientation of langmuir cells for misaligned winds and waves. *Journal of Geophysical Research*, 117, C05001. <https://doi.org/10.1029/2011JC007516>
- Verney, R., Lafite, R., Brun-Cottan, J. C., & Le Hir, P. (2011). Behaviour of a floc population during a tidal cycle: laboratory experiments and numerical modelling. *Continental Shelf Research*, 31(10), S64–S83.
- Von Smoluchowski, M. (1916). Drei vortrage über diffusion. brownsche bewegung und koagulation von kolloidteilchen. *Zeitschrift für Physik*, 17, 557–585.
- Warner, J. C., Armstrong, B., He, R., & Zambon, J. B. (2010). Development of a coupled ocean-atmosphere-wave-sediment transport (coawst) modeling system. *Ocean Modelling*, 35(3), 230–244.
- Warner, J. C., Sherwood, C. R., Signell, R. P., Harris, C. K., & Arango, H. G. (2008). Development of a three-dimensional, regional, coupled wave, current, and sediment-transport model. *Computers & Geosciences*, 34(10), 1284–1306.
- Waterson, N. P., & Deconinck, H. (2007). Design principles for bounded higher-order convection schemes—a unified approach. *Journal of Computational Physics*, 224(1), 182–207.
- Winterwerp, J. (2002). On the flocculation and settling velocity of estuarine mud. *Continental Shelf Research*, 22(9), 1339–1360.
- Winterwerp, J. C. (1998). A simple model for turbulence induced flocculation of cohesive sediment. *Journal of Hydraulic Research*, 36(3), 309–326.
- Winterwerp, J. C., & Van Kesteren, W. G. (2004). *Introduction to the physics of cohesive sediment dynamics in the marine environment*, (Vol. 56). Elsevier.

- Xu, F., Wang, D.-P., & Riemer, N. (2008). Modeling flocculation processes of fine-grained particles using a size-resolved method: comparison with published laboratory experiments. *Continental Shelf Research*, 28(19), 2668–2677.
- Xu, F., Wang, D.-P., & Riemer, N. (2010). An idealized model study of flocculation on sediment trapping in an estuarine turbidity maximum. *Continental Shelf Research*, 30(12), 1314–1323.
- Yang, D., Chen, B., Chamecki, M., & Meneveau, C. (2015). Oil plumes and dispersion in langmuir, upper-ocean turbulence: Large-eddy simulations and k-profile parameterization. *Journal of Geophysical Research: Oceans*, 120, 4729–4759. <https://doi.org/10.1002/2014JC010542>
- Yu, X., Ozdemir, C., Hsu, T.-J., & Balachandar, S. (2013). Numerical investigation of turbulence modulation by sediment-induced stratification and enhanced viscosity in oscillatory flows. *Journal of Waterway, Port, Coastal, and Ocean Engineering*, 140(2), 160–172.
- Zhang, J.-j., & Li, X.-Y. (2003). Modeling particle-size distribution dynamics in a flocculation system. *AICHE Journal*, 49(7), 1870–1882.